Petrology, mineralogy, and geochemistry of the olivine diogenite NWA 4255: new insights into the magmatic evolution of asteroid 4 Vesta

Ratiba Kared, Bertrand N. Moine, Abdelmadjid Seddiki, Jean Yves Cottin, Richard Greenwood, Ian A Franchi

HAL Id: hal-02402492

https://uca.hal.science/hal-02402492

Submitted on 10 Dec 2019

1 **Petrology, mineralogy, and geochemistry of the olivine diogenite NWA 4255: new**

2 **insights into the magmatic evolution of asteroid 4 Vesta**

3

4 Ratiba Kared1 & Bertrand N. Moine2 & Abdelmadjid Seddiki1 & Jean Yves Cottin2 &

5 Richard C. Greenwood3 & Ian A. Franchi3

6

7 1 Laboratoire Géoressources et Risques Naturels (GEOREN); Oran2 University, BP: 1510,

8 31000 Oran, Algeria

9 2 Magmas & Volcanoes Laboratory UMR6524 CNRS, Lyon University, UJM, Saint-Etienne,

10 France

11 3 Planetary and Space Sciences, Department of Physical Sciences, The Open University,

12 Walton Hall, Milton Keynes MK7 6AA, UK

13

16

17

18 **Abstract**

19 Northwest Africa (NWA) 4255 is a meteorite found in the region of Tindouf (southwestern

20 Algeria), classified as brecciated olivine diogenite. Based on textural observations and

21 orthopyroxene compositions, two different lithologies were determined: harzburgitic and

22 orthopyroxenitic. The orthopyroxenitic lithology contains orthopyroxene (Mg no. 73.99–

23 75.68) and spinel (Cr no. 83.09–85.11, Mg no. 15.57–22.45). On the other hand, the

24 harzburgitic lithology contains orthopyroxene (Mg no. 74.54–77.14) and olivine (Mg no.

25 70.94–72.57). The iron metal and the sulfides (Troilites) of this sample are present in both

26 lithologies and are low in Ni (Ni < 0.1wt%). The Fe/Mn ratio of orthopyroxenes ranges from

27 22.28 to 32.64 and show a large overlap between both lithologies. Lowest ratios are unusual;

28 they are below the defined field for diogenites and olivine diogenites. Δ17O values are −

29 0.234 ± 0.003 (1σ) and confirm that the NWA 4255 originated from 4Vesta. The results of

30 this study show that there is a genetic linkage between the two lithologies of NWA 4255 and

31 correspond to in situ crystallization processes. This olivine diogenite reflects transition

32 between two major magmatic processes in 4Vesta. The magma ocean of 4Vesta crystallized at

33 equilibrium, allowing the formation of a dunitic and harzburgitic mantle. This late lithology is

34 linked to the peritectic reaction between the olivines formed and the evolved liquid. Our

35 sample then reflects this crucial step of separating this mantle from the residual liquid. This
36 melt evolving on the peritectic allowed the formation of the observed harzburgitic assemblage
37 and then evolves out from the peritectic reaction to proceed to a fractional crystallization
38 process involving the formation of orthopyroxenite.
39

Introduction

41 The HED (Howardite, Eucrite, Diogenite) group of meteorites likely originated from the
42 Asteroid 4Vesta (Drake 2001). Diogenites are predominantly orthopyroxene-rich cumulates
43 (Krawczynski et al. 2008; Mandler and Elkins-Tanton 2013). However, recently, olivine
44 diogenites have been recognized as an important subset of diogenites and are considered to
45 represent the most primitive material within this subgroup (Krawczynski et al. 2008). The
46 designation olivine diogenite has been used for diogenites containing a considerable range of
47 modal olivine contents, from trace to 50 wt.% olivine (Bowman et al. 1997; Irving et al. 2009;
48 Mittlefehldt 1994; Sack and Ghiorso 1991; Shearer et al. 2010). However, when the olivine
49 abundance is between 1 and 5%, the most appropriate term is olivine-bearing diogenites
50 (Shearer et al. 2010). Diogenites, olivine-bearing diogenite, and olivine diogenites are
51 petrogenetically associated with basaltic magmatism linked to the earliest stages of
52 asteroidalmelting on the parent body of the Howardite–Eucrite–Diogenite (HED) meteorites
53 (Shearer et al. 2010). As pointed out by Mittlefehldt (2000), the origin of the parental magmas
54 of diogenites remains poorly understood. In this study, we look in detail at the origin and
55 interrelationship between two distinct lithologies present in the olivine diogenite NWA 4255.
56 We examine the major processes responsible for their genesis using petrology, mineral
57 chemistry, and whole-rock geochemistry. In particular, we examine whether the two
58 lithologies are co-genetic. Using the evidence from modeling studies, we investigate the
59 relationship between diogenites and olivine diogenites and assess how NWA 4255 fits into
60 the magmatic history of 4Vesta. Finally, we use the information gained from this detailed
61 study of NWA 4255 to examine the differentiation and crystallization history of vestian
62 magma ocean.
63

Petrography and texture

65 NWA4255 is an olivine diogenite discovered in 2002 in the Algerian Sahara. It is in the form
66 of many fragments (Fig. 1a) totalling a mass of 6 kg. Some fragments show a thin fusion
67 crust. Iron oxide is observed on some fragments, which reflects a supergene alteration of iron
68 metal. The study concerns seven fragments of this meteorite. NWA4255 is a brecciated

olivine diogenite. Observations under optical microscope (reflected light) and electron microscope allowed to highlight the presence of two lithologies, one contains olivine and is designated here as being the **"harzburgitic lithology,"** and the other is olivine free and is designated here as being the **"orthopyroxenitic lithology."** Iron metal and sulfides are present in small amounts as interstitial grain or tiny inclusions in orthopyroxene. Clinopyroxene is present as traces associated with iron metal within large orthopyroxene grains. The **"orthopyroxenitic lithology"** consists of orthopyroxene, spinel, sulfide, and scarce clinopyroxene (see below) (Figs. 1 and 2). This olivine diogenite consists of orthopyroxene (91.62%), olivine (6.79%), chromium spinel (1.08%), and trace of sulfide and iron metal. One of the most interesting features of the NWA 4255 is the presence of many small vugs in orthopyroxene and occasionally in the spinel in the orthopyroxenitic lithology. These vugs are associated with strings of sulfide and spinel inclusions (Fig. 1b, c).

Orthopyroxenitic lithology

Orthopyroxene

Orthopyroxene occurs as subhedral grains exhibiting a wide range of sizes (~8 to 0.01 mm in length) (Fig. 1d). In most cases, these grains are highly brecciated and are presumably fragments of much larger crystals. The original magmatic boundaries between orthopyroxene and spinel are sometimes preserved. In addition, clinopyroxene is also present and occurs as very small grains (~ 50 μm). It is associated with iron metal in orthopyroxene.

Chromium spinel

Spinel has several habitus and microstructures. Most spinels occur as subhedral to anhedral grains with a size of 100 to 600 μm. These spinel grains are highly brecciated when they are within or in contact with orthopyroxene (Fig. 1e). However, some spinels are euhedral (300 to 550 μmin diameter) showing igneous contacts with orthopyroxene (Fig. 1f). In addition, some small spinel grains are associated with sulfides (Fig. 2a). These grains often display curved contacts with orthopyroxene grains. Furthermore, there are spinels that form tiny inclusions (< 10 μm) and are associated with numerous vugs and sometimes with sulfides along cleavage planes within orthopyroxene grains.

Sulfides

Sulfides are more abundant in the orthopyroxenitic lithology. They are less common in the harzburgitic lithology. The shape and the grain size of sulfides are largely variable; some are

103   subhedral (~ 360 **μ**m in diameter) (Fig. 2b). Others are euhedral (20 to 50 **μ**m), and most were

104   observed as tiny grain inclusions within orthopyroxene and spinel.

105

106   **Harzburgitic lithology**

107   **Orthopyroxene**

108   Orthopyroxenes are essentially subhedral, varying in size to 2 mm to 1.5 cm in the longest

109   dimension (Fig. 3a). Most orthopyroxene grains are fractured and contain numerous olivine,

110   chromium spinel, ironmetal, and sulfide inclusions. In brecciated areas, pyroxenes are small

111   and display angular shapes, and range in size from 10 to 250 **μ**m. There are some

112   orthopyroxenes found exceptionally as inclusions in olivine. These orthopyroxenes can be up

113   to 200 **μ**m in longest dimension; they are anhedral with irregular boundaries (Fig. 3b and c).

114

115   **Olivine**

116   Olivine occurs only in harzburgitic lithology. It displays a heterogeneous distribution

117   occurring as millimeter-sized fragmented crystals, locally displaying original contacts with

118   orthopyroxene grains. Olivine grains are anhedral, ranging in size from 250 **μ**m to 1.5 mm

119   (Fig. 3a). Some small rounded grains of olivine (25–70 **μ**m) are occasionally found as

120   inclusions within large orthopyroxenes (Fig. 3e and f).

121

122   **Iron metal**

123   Iron metal is not abundant in NWA 4255, occurring as irregularly shaped grains associated

124   with orthopyroxene and sometimes with olivine. The iron grains can be as much as 500 **μ**min

125   diameter; these larger grains (Fig. 3f) have a halo of infiltrations in cracks of surrounding

126   orthopyroxene and olivine. Metallic iron is also in the form of very small grains (less than 10

127   **μ**m), associated with sulfides and spinels in the form of trails of inclusions in orthopyroxene.

128

129   **Analytical techniques**

130   Analyses of major and trace elements in various mineral phases were carried out using the

131   electron microprobe and by LA-ICP-MS (laser-ablation inductively coupled plasma mass

132   spectrometer). Image of the rock fragment presented in this work is a mosaic image

133   corresponding to an accumulation of 28 images obtained using a scanning electron

134   microscope (Jeol JSM-5910 LV) equipped with a PGT Spirit microanalysis system. Whole-

135   rock major and trace element analysis and oxygen isotope analyses were undertaken on two

136   fresh fragments of NWA 4255 weighing 1.56 g and 1.57 g (Aliquot 1 and Aliquot 2). These

137   were crushed and pulverized in an agate mortar before determining the concentrations of the

138   major and trace elements of the whole rock.

139

140   **Mineral phases major and trace element analyses**

141   Major and minor element chemistry of mineral phases was determined using an electron

142   microprobe (CAMECA SX 100, 15 kV, 20 nA), at Magmas and Volcanoes laboratory

143   (LMV)–Clermont-Ferrand-France. Standards were natural and synthetic minerals; ZAF

144   corrections were applied. The limit of detection of the electron microprobe analyses is LOD =

145   50–100 ppm depending on the element concerned. Trace element compositions were acquired

146   by a LA-ICP-MS (laser-ablation inductively coupled plasma mass spectrometer) at the LMV,

147   France, using a RESONETICS RESOLUTION M-50 laser powered by an ultra-short pulse

148   ATL ATLEXEXCIMER laser system. Operating conditions were of 193 nm wavelength, 73

149   μm spot diameter, associated to a repetition rate of 6 Hz. The sample was ablated in a He

150   atmosphere using a 193-nm wavelength laser computer-controlled and equipped with anATL

151   laser with ultra-short pulse duration (< 4 ns). Acquisition time was 90 s for background and

152   60 s for signal. The international standards NIST612 and BCR2 (Columbia River Basalt)

153   were used as external calibration standards. Four analyses were performed on these standards

154   before and after each data collection set. Si and Cr determined by electron microprobe are

155   used as internal standards to normalized concentration. The detection limits of all the

156   elements analyzed are less than 1 ppb. Reproducibility and accuracy of the analyses was

157   estimated through repeated analyses of BCR-2g standard at the beginning and at the end of

158   every run. Data reduction was carried out using the software package GLITTER (Van

159   Achterberg et al. 2001). For each analysis, the time resolved signal for each element was

160   monitored to discard perturbations related to inclusions, fractures or mixing.

161

162   **Whole-rock major and trace element analyses**

163   Two different techniques were used for major elements analysis. As for the first, a powdered

164   sample (108 mg) of the Aliquot 1 was taken, from which a small fraction (about 5 mg) was

165   deposited on a platinum wire and heated to 1580 °C in air. The molten glass was quenched in

166   water. The glass beads obtained were then analyzed by electron microprobe. These glass

167   beads were prepared at the CRPG Nancy- France, and then analyzed by electron microprobe

168   at the LMV-France. In this work, we present the average of three analyses that were made on

169   each three beads made. For the second technique, 100 mg of both aliquots (1 and 2) were

170   taken to perform the major element analyses using the alkaline fusion method with LiBO2

171 (1:3 dilution). One hundred milligrams of each extracted powder was mixed with 300 mg of

172 lithium metaborate (LiBO2). The mixture was then placed in a graphite crucible (25 mm in

173 diameter) and heated for 5 min in a magnetic induction furnace to 2KW (1100 °C). The glass

174 obtained was mixed with 50 ml of HNO3 1 M solution in a polystyrene bottle. The glass bead

175 was dissolved by the acid, then the solution obtained is filtered through a filter paper and

176 recovering all with deionized water in a volumetric flask of 200 ml. The final solutions were

177 analyzed by ICPAES (inductively coupled plasma atomic emission spectroscopy) at the

178 LMV-France, and analytical conditions were as follows: incident power = 1050 W, reflected

179 power < 5 W, Drainage = 0.31/min. BHVO-2 external standard was used as reference to

180 control accuracy and deviation. The results obtained by these two different methods are

181 consistent within analytical uncertainty (Table 7). Whole-rock trace element compositions

182 were analyzed by inductively coupled plasma mass-spectrometry (ICP-MS) at LMV on

183 Agilent 7500 cx. One powder sample of both aliquots (Aliquot 1: 98.4 mg and aliquot 2:

184 100.28 mg) was taken for trace element analysis. For dissolution, each powder sample was

185 dissolved in a mixture solution: 1 ml 20N of HF and 1 ml of 20N HNO3 in a 12-ml

186 Savillex™. The closed Savillex™ were placed on a hotplate at 100 °C for 48 h. The samples

187 were evaporated at 70 °C. After evaporation, a second attack is carried out with a mixture of 1

188 ml of 30 N HCl, 4 ml of 20 N HF, and 1 ml of HClO4 and heated at 100 °C for 2 days. This

189 step is followed by evaporation at 150 °C. A third attack with a mixture of 1 ml 30 N HCl, 4

190 ml 20 N and 1 ml HClO4 was carried out. The solution was then allowed to evaporate at 150

191 °C. The residue was dissolved in 2 ml 6 N HCl, then evaporated until all the HClO4 had been

192 removed. The residue obtained is dissolved with recovery 10 ml 0.4 N HNO3 and diluted

193 before analyzing. Two blanks followed the same protocol as the sample to confirm that the

194 NWA 4255 had not been contaminated during handling. Three mafic and ultramafic

195 international standards (BIR1, BCR2 et JP1) were used as calibration external standards. Fifty

196 milligrams of powder of aliquot 1 was sent to Montpellier University to check the reliability

197 of the data. The results obtained in the two laboratories by the solution- ICP-MS are

198 consistent within analytical uncertainty (Table 7).

199

200 **Oxygen isotopes analyses**

201 Oxygen isotopes analysis was undertaken on both NWA 4255 aliquots (aliquot 1 and aliquot

202 2, Table S1). Both aliquots were homogenized, and 2 mg of these powders was then loaded

203 for oxygen isotope analysis at the Open University, using an infrared laser-assisted

204 fluorination system (Miller et al. 1999; Greenwood et al. 2017). Each of the two lithologies

205 were analyzed in duplicate. The powders were heated in the presence of BrF5. After

206 fluorination, the released oxygen gas was purified by passing it through two cryogenic

207 nitrogen traps and over a bed of heated KBr. Oxygen gas was analyzed using a MAT 253 dual

208 inlet mass spectrometer. System precision, as defined by replicate analyses (n = 39) of our

209 internal obsidian standard, is ± 0.05‰for **δ**17O, ± 0.09‰for **δ**18O, ± 0.02‰for **Δ**17O (2**σ**).

210 Oxygen isotope analyses are reported in standard **δ** notation, where **δ**18O has been calculated

211 as: **δ**18O = [(18O/16O)sample/(18O/16O)ref − 1] Å~ 1000 (**‰**) and similarly for **δ**17O using

212 the 17O/16O ratio, the reference being vSMOW: Vienna Standard Mean Ocean Water. **Δ**17O,

213 which represents the deviation from the terrestrial fractionation line, has been calculated using

214 the linearized format of Miller (2002): **Δ**17O . 1000ln _1 fl **δ**17O=1000_−**λ** 1000ln _1 fl

215 **δ**18O=1000_ where **λ** = 0.5247, determined using 47 terrestrial whole rock and mineral

216 separate samples (Miller 2002; Miller et al. 1999).

217

Mineral chemistry: major and trace elements

219 Representative major element concentrations for orthopyroxene, chromite, and olivine are

220 summarized in Tables 1, 2, and 3, respectively. The iron metal data compositions are given in

221 Table 4, and the sulphide data are summarized in Table 5. The trace element concentrations

222 for these silicates are listed in Table 6. This olivine diogenite has two distinct populations of

223 both orthopyroxene and olivine (Figs. 4 and 5). This bimodal distribution reflects the fact that

224 two distinct lithologies are present in NWA 4255.

225

Orthopyroxenitic lithology

Orthopyroxene

228 Based on the terms ferroan and magnesian used by Beck and McSween (2010),

229 orthopyroxene in the orthopyroxenitic lithology show mainly a ferroan trend with a

230 composition ranging from (Wo1 En73 Fs24) to (Wo2 En75 Fs26) (Table 1) and with Fe no.

231 molar values of 24.32–26.01. These orthopyroxenes show concentrations with a slight

232 variability for Al2O3 (0.04–0.2 wt%), Cr2O3 (0.2–0.4 wt.%), and CaO (0.68–0.89 wt.%).

233 TiO2 concentrations are very low and often below the detection limit of the electron

234 microprobe and never exceed 0.07 wt.%. The Fe/Mn ratio of these orthopyroxenes varies

235 from 23.91 to 32.64. Trace element concentrations determined by LA-ICP-MS display very

236 limited variations in orthopyroxene from orthopyroxenitic lithology. Ti ranges from 255 to

237 276 ppm, Co from 5.01 to 5.56 ppm, Sc from 12.1 to 13.4 ppm and V from 109 to 117 ppm.

238 Remarkably, Ni concentrations are very low (0.254–0.386 ppm). The high field strength

239   element (HFSE) contents are 0.003–0.007 ppm for Hf and 0.025–0.040 ppm for Nb. Zr varies

240   in concentrations from 0.085 to 0.217 ppm. Ta is below detection limits (less than 0.5 ppb).

241   Moreover, incompatible trace element concentrations are very low with small variations in Y

242   (0.094 to 0.145 ppm) and Yb (0.027–0.034 ppm). As a consequence, in the ferroan

243   orthopyroxenes, no correlation is observed between these elements and Ti. The REE contents

244   are depleted relative to CI chondrite (Anders and Grevesse 1989). Moreover, the light REE

245   contents are generally depleted relative to heavy REE (La/Yb ranges from 0.03 to 0.08). On

246   the other hand, middle REEs are enriched (LaN/SmN = 0.07–0.28 and SmN/YbN = 0.30–

247   0.48). They show troughs at Eu in CI-normalized diagrams with a low Eu/Eu* ranging from

248   0.35 to 0.66 (Fig. 6). Although orthopyroxene from the two lithologies show REE patterns

249   that are sub parallel, the REE contents of orthopyroxene from the orthopyroxenitic lithology

250   are more enriched, especially for the MREE and HREE (SmN/YbN = 0.43–0.48) to those

251   obtained on harzburgitic lithology (Fig. 6).

252

253   **Chromite**

254   Spinels are magnesio-chromite (Usp1-2Sp15-16Chr81–84) with very high Cr no. values =

255   0.83–0.85 (Table 2). The Mg# values of chromite show significant variation, from 15.57 to

256   22.45. They contain minor amounts of TiO_2 (0.3–0.6 wt.%). The ranges of Cr# in this study

257   are similar to those previously reported for NWA1877 by Irving et al. (2005) (Fig. 7).

258   Magnesio-chromites exhibit variable trace element concentrations: V (5369 to 5471 ppm), Ti

259   (3462 to 3639 ppm), Co (7.81 to 10.47 ppm), Sc (5.16 to 6.39 ppm), and Ni (0.13 to 0.50

260   ppm). The Zr, Hf, Nb, and Ta contents range respectively from 3.83 to 3.93 ppm, 0.019 to

261   0.054 ppm, 3.67 to 3.93 ppm, and 0.002 to 0.008 ppm. Y ranges from 0.016 to 0.019 ppm.

262

263   **Harzburgitic lithology**

264   **Orthopyroxene**

265   Orthopyroxene is magnesian (Wo2En73-76Fs23–25) with Fe no. (in molar) ranging from

266   22.86 to 25.46. Minor element concentrations are slightly more depleted than those from

267   orthopyroxenitic lithology Al2O3 (0.08–0.4 wt.%), CaO (0.06–0.3 wt.%), Cr2O3 (0.6–0.9

268   wt.%), TiO_2 contents are up to 0.09 wt.%, but sometimes fall below detection limits. The

269   scarce orthopyroxene inclusions in olivine are magnesian (Mg no. 76.68 to 76.92) and show

270   the lowest Al2O3 (0.13 to 0.17 wt.%), CaO (0.67 to 0.73 wt.%) contents, the highest Cr2O3

271   (0.11 to 0.18 wt.%) contents among the orthopyroxene analyzed in NWA 4255.

272   Concentrations of Ti (207–260 ppm), V (91–124 ppm), Co (5.81–25.8 ppm), Sc (9.50–13.3

ppm), Ni (0.37–4.2 ppm), and Zr (0.029–0.103 ppm) exhibit slight variation. The contents Hf and Nb range to 0.002 to 0.004 ppm and to 0.024 to 0.036 ppm, respectively. Ta is below detection limits (less than 0.5 ppb). Incompatible trace element concentrations are 0.053–0.087 ppm Y and 0.017–0.022 ppm Yb. Sc, V, and Y have a positive correlation with Ti. Sc and Ti show a clear correlation between overlapping harzburgitic and orthopyroxenitic lithologies (Fig. 5), but both show a similar trend indicating that Ti has the same behaviour as Sc when partitioning between mineral and melt. This implies that the Ti has probably a + 3 valence as the Sc in this system. The REE patterns of orthopyroxene in the harzburgitic lithology are also depleted in LREE compared to HREE. La/Yb ranges from 0.05 to 0.16 and is lower than in orthopyroxenes of orthopyroxenitic lithology (Fig. 6). Eu/Eu* = 0.43–0.55, SmN/YbN ranges from 0.26 to 0.36 and LaN/SmN ratio from 0.18 to 0.64.

Olivine

Olivine also displays a bimodal distribution, Fe no. ranges from 27.43 to 29.06 for large grains and to 28.39 to 32.01 for small grains (Fig. 4). These values agree well with the compositions from olivine-bearing diogenites (Shearer et al. 2010). The Fe/Mn ratio displays wide variation from 38.8 to 72.7. The abundance of minor elements is very low and below detection limit of the electron microprobe. On the basis of LA-ICP-MS measurements of olivine from harzburgitic lithology, Ti ranges from 38.04 to 48.70 ppm, and Ca contents range from 315 to 1215 ppm. Ni and Co contents of olivine show a wide variation Ni (2.94 to 23.15 ppm) vs. Co (17.8 to 133 ppm). Ni exhibits a positive correlation with Co as shown in (Fig. 8), with a mean Ni/Co ratio of 0.26. V contents in these olivines yield concentrations ranging from 14 to 16.1 ppm and Sc in the range 3.73 to 4.1 ppm. In addition, Zr content is 0.019 ppm, and Nb concentrations range from 0.002 to 0.007 ppm. Hf and Ta contents are below detection limits. Y contents vary from 0.003 to 0.016 ppm and Yb contents from 0.002 to 0.007 ppm.

In all lithologies from NWA 4255

Iron metal and sulphides

In both lithologies fromNWA 4255, iron metal displays a very low Ni content (Ni < 0.1 wt%) and Co content ranges from 0.27 to 0.59 wt.% (Table 4). The mean Ni/Co ratio is similar to the olivine ratio (0.26) and extends the observed correlation. Sulfides are troïlite (FeS) with a very low content of transition metals, generally below the detection limit of the electron microprobe (Table 5). Furthermore, Troïlite inclusions in chromite are Cr-rich (1.57–3.43

307   wt%). Cr2O3 and CaO increase with Al2O3 in the orthopyroxene of both lithologies and

308   show a broad correlation from harzburgitic orthopyroxene to orthopyroxenitic

309   orthopyroxenes, with an overlap between them. On the other hand, major and minor element

310   abundances show a narrow overlap between magnesian and ferroan orthopyroxene. The

311   Fe/Mn ratio in orthopyroxene of both lithologies shows a wide overlap (Fe/Mn 22.28–30.94

312   and 23.91–32.64 for magnesian orthopyroxenes and ferroan orthopyroxenes respectively).

313   Whatever, the lithology Sc, Y, and V correlates with Ti. These variation trends are more

314   evident in harzburgitic lithology and differ from those in the literature (Fowler et al. 1995;

315   Shearer et al .2010). Compared with diogenitic orthopyroxenes discussed in the literature,

316   orthopyroxenes in NWA 4255 display very low trace element contents and are among the

317   poorest in compatible and trace elements. This evidence supports the possibility that these

318   orthopyroxenes crystallized from a very primitive melt. Orthopyroxenes from harzburgitic

319   lithology and containing olivine inclusions display intermediate compositions between

320   orthopyroxene include in olivine and orthopyroxene from orthopyroxenitic lithology. This

321   reinforces the idea that there is a co-genetic link between the both lithologies.

322

323   **Whole-rock geochemistry**

324   The whole-rock data for NWA 4255 are listed in Table 7. Chondrite CI-normalized rare earth

325   elements patterns show that NWA 4255 has a flat shape for light and intermediate rare earth

326   elements. The La varies from 125 ppb CI to 258 ppb CI, and the YbN varies from 203 ppb CI

327   to 231 ppb CI. They are highly depleted in comparison with CIs, especially for LREEs and

328   MREEs ((La/Sm)N = 0.19–0.64). They show Eu troughs with a low average Eu/Eu*

329   (EuN/(SmN*GdN)1/2) ratio of 0.47. The Ce/Ce* (CeN/(LaN*PrN)1/2) ratios range from 0.97

330   to 1.02. The NWA 4255 has Fe no. (Fe/(Fe + Mg)) of 25.88. The average Fe/Mn ratio is

331   28.93. Average concentrations for Sc and Ti are 12 and 263 ppm, respectively. It should be

332   noted that the data shows troughs at Th and Pb and peaks at Ba, U, and Ti (Fig. 9).

333

334   **Oxygen isotope analysis**

335   Duplicate analyses of both of the two main lithologies in NWA 4255 gave essentially

336   identical results within error, with the harzburgite having the composition: $\delta^{17}O$ = 1.675 ±

337   0.007‰ (2σ), $\delta^{18}O$ = 3.642 ± 0.016‰ (2σ), $\Delta^{17}O$=− 0.234 ± 0.001‰ (2σ) and the

338   orthopyroxenite: $\delta^{17}O$ = 1.682 ± 0.016‰ (2σ), $\delta^{18}O$ = 3.656 ± 0.010‰ (2σ), $\Delta^{17}O$=− 0.234

339   ± 0.010‰(2σ) (Table S1). Both lithologies have$\Delta^{17}O$values that are close to the mean $\Delta^{17}O$

340   value of − 0.241 ± 0.018 ‰ (2σ) obtained by Greenwood et al. (2017) for 105 eucrite and

341 diogenite analyses, both falls and finds. This indicates that the harzburgite and
342 orthopyroxenite lithologies in NWA 4255 are both normal members of the HED suite.
343

Discussion

Phase equilibria

346 On the diagram of Fe# Opx versus Fe#. Olivine (Fig. 10), couples of compositions of olivines
347 and orthopyroxenes with textural equilibrium (original magmatic boundaries) are represented.
348 These data fall almost exactly on the equilibrium line, defined by Mittlefehldt (1994).
349 Olivines and orthopyroxenes from Harzburgitic lithology are in chemical equilibrium. We
350 distinguish a progressive chemical evolution in the NWA 4255, with an iron enrichment when
351 the olivine grains become smaller and smaller and scarcer and scarcer. This reflects both the
352 progressive differentiation of the magma and the advancement of the peritectic reaction
353 consuming the olivine. This suggests that during magmatic evolution and peritectic reaction,
354 the phase's compositions remained in equilibrium. This observation is in contradiction with
355 the results of Beck and McSween (2010) whose brecciated samples show erratic Fe# Opx
356 versus Fe#. Olivine compositions. They interpret this as evidence of an intimate mixture of no
357 cogenetic harzburgitic and diogenitic rocks by intense brecciation linked to meteorite impacts.
358 These evidences provide support for a genetic relationship between the various lithologies of
359 NWA 4255. Olivine, orthopyroxene, and iron metal of the harzburgitic and orthopyroxenitic
360 lithologies, as well as the whole-rock analysis, are aligned on the same evolution trend (Fig.
361 11). This shows that the whole rock is the mixture of these different phases. On the other
362 hand, the fact that the Ni/Co ratio is relatively constant supports the hypothesis of a co-
363 genesis of the different phases (Figs. 8 and 12). This low Ni/Co ratio seems linked to the very
364 low abundance of Ni in the melt at the origin of NWA4255. Moreover, some orthopyroxenes
365 in orthopyroxenitic lithology are slightly shifted to even lower values of Ni and deviate from
366 this trend. The abundance of sulfide inclusions in these orthopyroxenes may represent a sink
367 for this siderophile and chalcophilic element at the expense of orthopyroxene. The Cr/V ratio
368 in the orthopyroxene varies between 0.24 and 0.38. This ratio, based on the work of Cartier et
369 al. (2014), implies that the fO2 was well below Iron- Wustite buffer (IW-7). This is lower
370 than the estimates for diogenites and eucrites (IW-2) of Boesenberg and Delaney (1997).
371 Under these conditions, the iron metal could have been present as a liquidus phase. This metal
372 appears after the formation of the metal core that has probably a chondritic Ni/ Fe ratio, and it
373 originates from the differentiation of magma and the rapid attainment of iron saturation at

374   very low oxygen fugacity. This implies that the metal in NWA 4255 is not related to a metal-

375   rich precursor, and so was not chondritic metal brought in by impactors, but a metal

376   precipitate formed under liquidus conditions and in chemical equilibrium with the silicate

377   melt, as well as with both olivine and orthopyroxene.

378

Petrogenetic relationship between the two main lithologies present in NWA 4255

379

380   Firstly, the harzburgitic lithology consists of orthopyroxene, olivine, and iron metal. Olivine

381   shows an increase in Fe no. as its crystal size decreases. This most likely reflects a peritectic

382   reaction between olivine and melt to produce orthopyroxene In addition, the orthopyroxenitic

383   lithology consists of orthopyroxene and spinel but is devoid of olivine. It is also more

384   enriched in Fe no. than the harzburgitic lithology and display higher incompatible trace

385   element contents. This implies that the olivines reacting with the liquid along the peritectic

386   produce orthopyroxene, which shields the olivine and isolates it from the residual melt. The

387   liquid then evolves out of the peritectic and produces orthopyroxene and spinel by fractional

388   crystallization.

389

Evolution of minor and trace elements

390

391   The concentration of trace elements in NWA 4255 are slightly varied between the different

392   aliquots as is the case in other diogenites and olivine diogenites (Barrat et al. 2006; Fowler et

393   al. 1994, 1995; Mittlefehldt 1994, 2015; Shearer et al. 1997, 2010). These concentrations are

394   low compared with those known in the literature, implying that it is among the most primitive

395   or the less evolved diogenites. Despite this low content, we still observed positive correlations

396   between the Sc, V, and Y with Ti. This could be explained by a similar behaviour during

397   orthopyroxene crystallization linked to a change in the valence of titanium to 3+. This implies

398   that most of the Ti is present in the 3+ valence that it is coherent with the very low calculated

399   oxygen fugacity (IW-7). Note that these correlations are only observed in the harzburgitic

400   orthopyroxene, but not in the orthopyroxene of the orthopyroxenitic lithology. This could

401   imply that the harzburgitic lithology is more reduced than the orthopyroxenitic lithology

402   which is also supported by the presence of metal. In addition, the concentration of Yb and the

403   REEs increase from the harzburgitic to orthopyroxenitic lithology. This suggests that this is

404   linked to the decrease of melt mass, and that orthopyroxene in the orthopyroxenitic lithology

405   crystallized after the crystallization of harzburgitic orthopyroxene, as proposed by Beck et al.

406   (2013). Additionally, the REE patterns displayed by the orthopyroxenitic orthopyroxenes

407   have characteristic shapes (MREE enrichment) that are different from those of the

harzburgitic orthopyroxenes. The difference in shape of REE pattern indicates that the orthopyroxenes of orthopyroxenitic lithology are the strict product of mineralmelt equilibrium between chondritic melt and orthopyroxene, as confirmed by the Onuma diagram (Fig. S1). The REE pattern of orthopyroxene in harzburgitic lithology indicates a more complex mechanism involving a distribution of REE between olivine-orthopyroxene-melt and reflecting the peritectic reaction. The REE patterns show a progressive enrichment of middle and heavy rare earth elements from the harzburgitic orthopyroxene to the orthopyroxenitic orthopyroxene. This confirms the progress of the peritectic reaction between the minerals formed and the liquid involving more and more orthopyroxene and less and less olivine. When the liquid leaves the peritectic, it passes into the field of orthopyroxene + liquid resulting in the formation of orthopyroxene only (Fig. 12).

Petrogenesis of olivine diogenite and diogenite

Large grains of olivine are only observed in the harzburgitic lithology; they are more magnesian than the small grains. This implies that the most magnesian olivine crystals are consumed by the peritectic reaction and transformed into orthopyroxene (Fig. 12). Olivine and spinel show preservation of magmatic boundaries with orthopyroxene indicating that the primary relationship between the various lithologies in NWA 4255 was controlled by igneous events. In contrast, the brecciation that is commonly present in the sample represents a secondary process, which obviously occurred after the crystallization of the mineral phases. We propose that the two lithologies in this olivine diogenite (NWA 4255) are genetically linked; furthermore, they represent a continuation of a magmatic crystallization sequence that evolved from the harzburgitic to the orthopyroxenitic lithology. Additionally, this provides the most cogent evidence confirming that the association between the lithologies is not the result of brecciation, but instead represents a magmatic evolution in the olivine diogenite. The scheme presented here for NWA 4255 is in contrast to that proposed by Beck and McSween (2010) for their samples. These authors suggest that magnesian orthopyroxenes, ferran orthopyroxenes, and olivine in close proximity were not in chemical equilibrium, but instead represent the product of brecciation of a harzburgitic lithology and an orthopyroxenitic lithology that were then subsequently mixed to produce their samples (Fig. 10). The high ratio of Cr no. in the chromite of NWA 4255 (as NWA 1877 Diogenite) (Fig. 7) is previously interpreted as residual spinel from the mantle (Irving et al. 2005), precipitate from a primitive melt at chromium saturation according to Irvine (1977) and the chemical estimations of the silicate fraction of 4Vesta (Lodders 2000).

The Fe/Mn ratio

Fe/Mn ratio in orthopyroxenes of both lithologies varies from 22.28 to 32.64; in addition, it shows a large overlap between them. This ratio is different from what is known for diogenites (Beck and McSween 2010) but is similar to that seen in some olivine diogenites (Beck and McSween 2008) and other HED samples (Mayne et al. 2009). This leads us to raise the question about the Fe/Mn ratio and why it is so different despite the fact that NWA 4255 shows most of the diagnostic characteristics of a diogenite from 4Vesta. A different orthopyroxene Fe/Mn in olivine diogenites than in regular diogenite would suggest complex crystallization processes on 4Vesta (Beck and McSween 2008). Furthermore, the Ni/Co in olivine is also different in NWA 4255 compared to other diogenites (Fig. 8).

Oxygen isotopes

As discussed above, both the harzburgitic and orthopyroxenitic lithologies in NWA 4255 have closely similar oxygen isotope compositions. This supports the conclusions based on petrography and major and trace element geochemistry, indicating that the two major lithologies in NWA 4255 are genetically related to each other.

MELTS modelling

In this section, we use the model of Mandler and Elkins- Tanton (2013) to discuss the likely formation mechanism of the lithological variation observed in NWA 4255. We look at the differentiation and crystallization of the Vestian magmatic ocean, to see how NWA 4255 might be placed in the overall crystallization sequence. In particular, we focus on the formation of olivine diogenites and diogenites in general. We chose as our starting material the composition suggested by Boesenberg and Delaney (1997) for the bulk silicate composition of 4Vesta. However, our conclusions would be equally valid if we had chosen a different composition, such as those suggested by Dreibus and Wänke (1980), Lodders (2000); Ruzicka et al. (1997), as compiled by Mandler and Elkins-Tanton (2013). Since, all of these compositions are very similar to each other. We used as the starting conditions for our modelling: IW-7, T = 1622 °C, P = 100 bar (< 1 kb because this is the maximum pressure in the center of 4Vesta if we consider its diameter (530 km) and its average gravity (0.22 m/s2). Using the pMELTS software (Ghiorso et al. 2002), we calculated the compositions of the resulting solids and the modal proportion of each mineral phase. We controlled the liquid in each step and also the evolution of the liquid. We took the composition of the vestian magmatic ocean (Fig. 13, Liquid 1) which undergoes a crystallization rate of 70%. The 70%

476   solids formed (Fig. 13, solid 1) represent a harzburgitic mantle comprising 63% olivine
477   (Fo79), 36% orthopyroxene (Wo2En81Fs17), and 1% spinel (Mg no. 51.48 and Cr no. 72.86).
478   (Fig. 13). The solid mantle formed was separated, and the remaining 30% liquid was restarted
479   and cooled under the same equilibrium conditions. We are able to reproduce the modal and
480   chemical compositions of NWA4255 with 22% crystallization (solid 2). The stages of
481   crystallization at equilibrium of this liquid show that it evolves on the peritectic and produce
482   olivine diogenite (Fig. 13, liquid 2). Olivines react with liquid at peritectic and are consumed
483   partially or totally. When all the olivine has been consumed or isolated within the
484   orthopyroxenes, the liquid leaves the peritectic to enter the liquid + orthopyroxene field (Fig.
485   13, liquid 3). The evolution of the liquid at the level of the peritectic and the subsequent
486   passage through the "Opx + melt" field reflect the transition from equilibrium crystallization
487   to fractional crystallization. We obtained olivine diogenite (solid 2) containing 3.4% olivine
488   (Fe no. 30), 94% orthopyroxene (Fe no. = 74.86) and 2.3% spinel (Mg no. 39.21 and Cr no.
489   70.21) and traces of metal. This composition and the modal proportions of these minerals are
490   very similar to those actually measured in NWA 4255. The results of our modelling suggest
491   that NWA 4255 could be derived from the transition zone between the eucritic-diogenetic
492   crust and the mantle of his parent body. These results are consistent with those of Mandler
493   and Elkins-Tanton (2013).
494

495   **Outstanding issues**
496   The actual composition of spinel in NWA 4255 measured is Mg no. 15.3–22.4 and Cr no.
497   83.09–85.11, whereas the predicted values from the pMELTS calculations are (Mg no. 39.21
498   and Cr no. 70.21), which are significantly different. Thus, there is a problem in reproducing
499   the magmatic composition of spinel, whereas there was no problem in reproducing this for the
500   other silicates. According to the phase diagrams of basaltic systems at low pressure, there
501   should be no spinel (Mg-Al spinel) at equilibrium, the spinel stability field being far from our
502   compositions. However, the composition of the liquid particularly rich in Cr and Fe implies
503   the Cr saturation and the chromium spinel precipitation (Irvine 1977). It is possible that the
504   thermodynamic database of MELTS does not strictly cover these ranges of composition and
505   fugacity oxygen to reproduce spinel composition. Moreover, there are some differences
506   between NWA 4255 and the others HEDs, such as the wide range of variation of the low
507   concentration of Ni in the olivine. Therefore, the Ni/ Co in olivine of NWA 4255 is much
508   different from what is known in the literature, in addition to the low Fe/Mn ratio. At present,
509   there is no simple explanation for these discrepancies.

Conclusion

NWA 4255 displays two populations of orthopyroxene crystals as indicated by their major, minor, and trace element compositions. This distinction was also observed with respect to their texture. NWA 4255 is essentially composed of two lithologies: one containing olivine, which we have termed a harzburgite, and the other an olivine-free orthopyroxenite. A transitional lithology is present at the contact between these two main lithologies. This olivine diogenite is an extraction in transitional zone between two different lithologies from Vesta, and it has undergone a subsequent brecciation. Based on the petrographic observations and using chemical data for the modelling, we conclude that the two lithologies are genetically linked. Based on the results of our modelling studies, Vesta evolved first via the formation of a primitive harzburgitic mantle. As soon as this unit was formed, it was separated from the liquid by a fractional crystallization process. The remaining liquid continued to crystallize along the peritectic to form olivine diogenites and then evolved further to form the diogenite by the fractional crystallization. Finally, the harzburgitic and the orthopyroxenitic lithology are formed by the equilibrium crystallization (E.C) and the fractional crystallization (F.C), respectively. The NWA 4255 reflects transition between two different major magmatic processes in 4Vesta (E.C and F.C). The peritectic reactions are the link between these two processes. These lithologies come from the deepest zones of the crust, at the interface with the mantle.

543

References

544 Anders E,Grevesse N (1989) Abundances of the elements: meteoritic and solar. Geochim
546 Cosmochim Acta 53(1):197–214

547 Barrat JA, Beck P, Bohn M, Cotten J, Gillet P, Greenwood RC, Franchi IA (2006) Petrology
548 and geochemistry of the fine-grained, unbrecciated diogenite Northwest Africa 4215. Meteorit
549 Planet Sci 41(7):1045–1057

550 Beck AW, McSween HY (2008) Fe and Mn systematics in olivinebearing diogenites.
551 Abstract #1291, Lunar and Planetary Science XXXIX, USA

552 Beck AW, McSween HY (2010) Diogenites as polymict breccias composed of
553 orthopyroxenite and harzburgite: Diogenites as polymict breccias. Meteorit Planet Sci
554 45(5):850–872

555 Beck AW, McSween HY, Bodnar RJ (2013) In situ laser ablation ICP-MS analyses of dimict
556 diogenites: further evidence for harzburgitic and orthopyroxenitic lithologies. Meteorit Planet
557 Sci 48(6):1050–1059

558 Boesenberg JS, Delaney JS (1997) A model composition of the basaltic achondrite planetoid.
559 Geochim Cosmochim Acta 61(15):3205– 3225

560 Bowman LE, SpildeMN, Papike JJ (1997) Automated energy dispersive spectrometer modal
561 analysis applied to the diogenites. Meteorit Planet Sci 32(6):869–875

562 Cartier C, Hammouda T, Doucelance R, Boyet M, Devidal JL, Moine B (2014) Experimental
563 study of trace element partitioning between enstatite and melt in enstatite chondrites at low
564 oxygen fugacities and 5GPa. Geochim Cosmochim Acta 130:167–187

565 Drake MJ (2001) Presidential address: presented 2000 August 28, Chicago, Illinois, USA the
566 eucrite/Vesta story. Meteorit Planet Sci 36(4):501–513

567 Dreibus G, Wänke H (1980) The bulk composition of the Eucrite parent asteroid and its
568 bearing on planetary evolution. Z Naturforsch A 35(2)204–216

569 Fowler GW, Papike JJ, Spilde MN, Shearer CK (1994) Diogenites as asteroidal cumulates:
570 insights from orthopyroxene major and minor element chemistry. Geochim Cosmochim Acta
571 58(18):3921–3929

572 Fowler GW, Shearer CK, Papike JJ, Layne GD (1995) Diogenites as asteroidal cumulates:
573 insights from orthopyroxene trace element chemistry. Geochim Cosmochim Acta
574 59(14):3071–3084

575 Ghiorso MS, HirschmannMarcM, Reiners PeterW, Kress VC III (2002) The pMELTS: an
576 revision of MELTS aimed at improving calculation of phase relations and major element

577   partitioning involved in partial melting of the mantle at pressures up to 3 GPa. Geochem

578   Geophys Geosyst 3(5). https://doi.org/10.1029/2001GC000217

579   Greenwood RC, Barrat JA, Scott ERD, Haack H, Buchanan PC, Franchi IA, Burbine TH

580   (2015) Geochemistry and oxygen isotope composition of main-group pallasites and olivine-

581   rich clasts in mesosiderites: Implications for the "Great Dunite Shortage" and HED-

582   mesosiderite connection. Geochim Cosmochim Acta 169: 115–136

583   Greenwood RC, Burbine TH, Miller MF, Franchi IA (2017) Melting and differentiation of

584   early-formed asteroids: the perspective from high precision oxygen isotope studies. Chem

585   Erde-Geochem 77:1–43

586   Hahn TM, Lunning NG, McSween HY, Bodnar RJ, Taylor LA (2018) Mg-rich harzburgites

587   from Vesta: mantle residua or cumulates from planetary differentiation? Meteorit Planet Sci

588   53(3):514–546

589   Irvine TN (1977) Chrome spinel crystallization in the join Mg2SiO4- CaMgSi2O6-

590   MgCr2O4-SiO2. Carnegie Inst Washington Yearb 76: 465–472

591   Irving AJ, Kuehner SM, Carlson RW, Rumble D, Hupé AC, Hupé GM (2005) Petrology and

592   multi-isotopic composition of olivine diogenite nwa 1877: a mantle peridotite in the proposed

593   hedo group ofmeteorites. Abstract #2188 Lunar and Planetary Science XXXVI, USA

594   Irving AJ, Bunch TE, Kuehner SM, Wittke JH, Rumble D (2009) Peridotites related to

595   4vesta: deep crustal igneous cumulates and mantle samples. Abstract #2466. 40th Lunar and

596   Planetary Science Conference, USA

597   Krawczynski MJ, Elkins-Tanton LT, Grove TL (2008) Krawczynski 2008. Petrology of

598   mesosiderite(?) MIL03443,9; constraints on eucrite parent body bulk composition and

599   magmatic processes. Abstract #1229, 39 th Lunar and Planetary Science Conference, USA

600   Lodders K (2000) An oxygen isotope mixing model for the accretion and composition of

601   rocky planets. In: Benz W, Kallenbach R, Lugmair GW (eds) From dust to terrestrial planets,

602   vol 9. Springer Netherlands, Dordrecht, pp 341–354

603   Lunning NG, McSween HY, Tenner TJ, Kita NT, Bodnar RJ (2015) Olivine and pyroxene

604   from the mantle of asteroid 4 Vesta. Earth Planet Sci Lett 418:126–135

605   Mandler BE, Elkins-Tanton LT (2013) The origin of eucrites, diogenites, and olivine

606   diogenites: magma ocean crystallization and shallow magma chamber processes on Vesta.

607   Meteorit Planet Sci 48(11): 2333–2349

608   Mayne RG, McSween HY, McCoy TJ, Gale A (2009) Petrology of the unbrecciated eucrites.

609   Geochim Cosmochim Acta 73(3):794–819

610 Miller MF (2002) Isotopic fractionation and the quantification of 17O anomalies in the
611 oxygen three-isotope system: an appraisal and geochemical significance. Geochim
612 Cosmochim Acta 66(11):1881– 1889

613 Miller MF, Franchi IA, Sexton AS, Pillinger CT (1999) High-precision d17O isotope
614 measurements of oxygen from silicates and other oxides: methods and applications. Rapid
615 Commun Mass Spectrom 13: 1211–1217

616 Mittlefehldt DW (1994) The genesis of diogenites and HED parent body petrogenesis.
617 Geochim Cosmochim Acta 58(5):1537–1552

618 Mittlefehldt DW (2000) Petrology and geochemistry of the elephant moraine A79002
619 diogenite: a genomict breccia containing a magnesian harzburgite component. Meteorit Planet
620 Sci 35(5):901–912

621 Mittlefehldt DW (2015) Asteroid (4) Vesta: I. the howardite-eucritediogenite (HED) clan of
622 meteorites. Chem Erde-Geochem 75(2): 155–183

623 Righter K, Drake MJ (1997) A magma ocean on Vesta: core formation and petrogenesis of
624 eucrites and diogenites. Meteorit Planet Sci 32(6):929–944

625 Ruzicka A, Snyder GA, Taylor LA (1997) Vesta as the howardite, eucrite and diogenite
626 parent body: implications for the size of a core and for large-scale differentiation. Meteorit
627 Planet Sci 32(6):825–840

628 Sack RO, Ghiorso MS (1991) Chromian spinels as petrogenetic indicators: thermodynamics
629 and petrological applications. AmMineral 76: 827–847

630 Shearer CK, Fowler GW, Papike JJ (1997) Petrogenetic models for magmatism on the eucrite
631 parent body: evidence from orthopyroxene in diogenites. Meteorit Planet Sci 32(6):877–889

632 Shearer CK, Burger P, Papike JJ (2010) Petrogenetic relationships between diogenites and
633 olivine diogenites: implications for magmatism on the HED parent body. Geochim
634 Cosmochim Acta 74(16):4865–4880

635 Stopler E (1975) Petrogenesis of eucrite, howardite and diogenite meteorites. Nature
636 258:220–222

637 Toplis MJ, Mizzon H, Monnereau M, Forni O, McSween HY, Mittlefehldt DW, Russell CT
638 (2013) Chondritic models of 4 Vesta: implications for geochemical and geophysical
639 properties. Meteorit Planet Sci 48(11):2300–2315

640 Van Achterberg E, Ryan CG, Griffin WL (2001) GLITTER version 4 user's manual on-line
641 interactive data reduction for the LA-ICPMS microprobe. Macquarie Research Ltd, North
642 Ryde 71

643

Table 1   Representative microprobe analyses for orthopyroxene from NWA 4255 (in wt% oxides)

n°	6	28	19	27	42	3	50	8	16	57	41	58
Lithology	Harzburgitic							Orthopyroxenitic				
						Opx inclusion in olivine						
SiO$_2$	55.51	55.57	55.70	55.83	55.64	56.21	55.90	55.57	54.93	55.13	55.47	55.06
TiO$_2$	0.06	0.06	0.02	0.02	0.01	b.d.	0.07	0.07	0.11	0.04	0.04	0.09
Al$_2$O$_3$	0.17	0.33	0.27	0.31	0.31	0.13	0.16	0.35	0.33	0.40	0.29	0.36
Cr$_2$O$_3$	0.21	0.24	0.12	0.24	0.21	0.18	0.17	0.33	0.31	0.30	0.21	0.25
FeO	15.03	15.04	15.13	15.16	15.68	15.06	15.58	16.20	16.26	16.61	16.58	16.54
MnO	0.51	0.66	0.59	0.50	0.54	0.59	0.57	0.55	0.62	0.60	0.68	0.59
MgO	28.04	28.11	27.88	27.79	27.42	28.16	27.78	26.90	26.65	26.76	26.61	26.40
CaO	0.90	0.78	0.66	0.71	0.82	0.69	0.73	0.78	0.78	0.85	0.86	0.78
Na2O	0.11	0.01	0.02	0.00	0.04	0.03	0.02	0.02	0.00	0.00	0.04	0.03
K$_2$O	0.00	0.02	0.00	0.02	0.02	0.00	0.01	0.01	0.01	0.00	0.00	0.00
Total	100.54	100.83	100.39	100.58	100.68	101.05	100.99	100.79	100.00	100.69	100.79	100.12
Fe/Mn	29.17	22.28	25.47	29.90	28.41	25.10	26.72	28.92	26.02	27.21	24.03	27.42
Fe/Mg	30.06	30.02	30.45	30.60	32.08	30.01	31.46	33.78	34.23	34.81	34.96	35.15
Mg #	76.89	76.91	76.66	76.57	75.71	76.92	76.07	74.75	74.50	74.18	74.10	73.99
Wo %	1.75	1.51	1.29	1.39	1.59	1.33	1.42	1.54	1.55	1.67	1.70	1.55
En %	75.54	75.75	75.67	75.50	74.51	75.89	74.99	73.60	73.34	72.94	72.84	72.84
Fs %	22.71	22.74	23.04	23.10	23.90	22.78	23.59	24.86	25.10	25.39	25.46	25.61

Mg no. = Mg/(Mg + Fe) × 100. Fe/Mn and Fe/Mg are calculated from molar abundances

b.d. below detection limit

Table 2   Representative microprobe analyses for chromite of orthopyroxenitic lithology (in wt% oxides)

Fragment	50	52	44	11	19	16	3	15	4	10	20	13
SiO$_2$	0.02	0.05	0.07	0.00	0.00	0.14	0.02	0.00	0.02	0.01	0.01	0.00
TiO$_2$	0.37	0.46	0.56	0.57	0.63	0.52	0.51	0.62	0.54	0.64	0.49	0.35
Al$_2$O$_3$	7.94	7.68	7.43	7.27	7.29	6.96	7.21	7.07	7.22	7.15	7.13	7.13
Cr$_2$O$_3$	57.38	58.84	59.38	58.60	59.32	56.92	59.08	58.66	59.90	59.36	59.33	58.49
FeO	28.53	27.90	27.88	26.77	27.31	28.00	27.44	26.91	27.52	26.71	27.63	28.02
MnO	0.69	0.67	0.56	0.63	0.59	0.57	0.61	0.65	0.59	0.58	0.62	0.66
MgO	2.89	3.13	3.43	3.91	3.73	3.73	3.54	3.90	3.66	3.93	3.58	3.07
Total	97.82	98.74	99.30	97.75	98.87	96.85	98.41	97.86	99.44	98.41	98.79	97.72
Mg#	15.57	16.65	18.04	20.85	19.68	20.01	18.86	20.83	19.26	20.81	19.03	15.86
Cr#	82.90	83.71	84.29	84.39	84.53	84.59	84.61	84.76	84.77	84.78	84.80	84.83
Sp	15.42	16.07	15.43	15.29	15.18	14.78	15.11	14.88	14.97	14.95	14.89	14.90
Chrm	81.23	82.54	82.75	83.18	82.90	83.30	83.06	83.45	83.32	83.33	83.11	83.33
Usp	1.01	1.24	1.47	1.52	1.69	1.42	1.37	1.66	1.43	1.70	1.30	1.24

Mg no. = Mg/(Mg + Fe) × 100. Cr no. = Mg/(Mg + Fe) × 100 calculated from molar abundances

b.d. below detection limit

Table 3 Representative microprobe analyses for olivine from harzburgitic lithology (in wt% oxides)

Specific	Large grains							Small inclusions in opx				
n°	25	9	10	11	12	13	48	28	39	33	41	44
SiO_2	38.27	38.19	38.05	38.13	37.93	37.99	38.25	38.17	36.97	37.60	38.13	37.96
TiO_2	b.d.	b.d.	0.02	0.02	b.d.	b.d.	0.07	0.01	0.05	b.d.	b.d.	b.d.
Al_2O_3	b.d.	0.02	b.d.	b.d.	b.d.	0.02	0.02	b.d.	0.02	b.d.	0.01	b.d.
Cr_2O_3	0.01	b.d.	b.d.	b.d.	b.d.	b.d.	b.d.	b.d.	0.03	b.d.	b.d.	b.d.
FeO	25.08	25.30	24.90	25.16	24.99	25.31	25.94	26.22	28.07	26.87	26.53	26.98
MnO	0.47	0.48	0.52	0.52	0.52	0.46	0.60	0.67	0.61	0.59	0.60	0.60
MgO	36.80	36.68	36.91	37.06	37.08	37.00	36.21	35.60	34.68	35.50	35.26	35.36
CaO	0.06	0.01	0.03	0.04	0.02	0.02	0.01	0.06	0.07	b.d.	0.02	0.05
Na_2O	0.02	0.03	b.d.	0.03	b.d.	b.d.	b.d.	b.d.	b.d.	b.d.	b.d.	b.d.
Total	100.70	100.74	100.47	100.98	100.58	100.80	101.09	100.73	100.50	100.56	100.56	100.95
Fe/Mn	52.73	51.37	47.02	47.71	47.03	54.04	42.42	38.77	45.17	45.12	43.29	44.17
Mg#	72.34	72.10	72.55	72.42	72.57	72.27	71.33	70.76	68.77	70.19	70.32	70.02
Fa	27.66	27.90	27.45	27.58	27.43	27.73	28.67	29.24	31.23	29.81	29.68	29.98

Mg no. = Mg/(Mg + Fe) × 100. Fe/Mn and Fe/Mg are calculated from molar abundances

b.d. below detection limit

649
650

Table 4 Representative microprobe analyses of Iron metal from orthopyroxenitic and harzburgitic lithologies (wt% element)

Lithology	Orthopyroxenitic					Harzburgitic						
n°	3	12	23	25	15	7	19	16	17	20	19	30
Si	0.06	0.02	0.01	0.01	b.d.	0.02	b.d.	b.d.	0.01	b.d.	b.d.	b.d.
S	0.03	0.02	0.01	0.04	b.d.	0.01	b.d.	0.01	0.01	b.d.	b.d.	0,01
Fe	98.16	98.68	99.04	99.36	99.41	99.59	99.74	99.75	99.75	99.83	99.83	99.83
Co	0.45	0.46	0.51	0.49	0.28	0.30	0.41	0.34	0.34	0.38	0.39	0.42
Ni	0.14	0.12	b.d.	0.13	0.10	b.d.	0.09	b.d.	b.d.	b.d.	0.11	b.d.
Mg	b.d.	b.d.	b.d.	0.01	0.01	b.d.	b.d.	0.01	0.01	0.01	b.d.	b.d.
Mn	0.05	0.04	0.03	0.01	b.d.	0.01	b.d.	0.01	b.d.	0.02	0.01	b.d.
Cr	0.09	0.05	0.07	0.02	b.d.	0.02	b.d.	0.01	0.11	0.59	0.02	b.d.
Total	98.98	99.39	99.76	100.05	99.80	99.99	100.24	100.15	100.27	100.86	100.36	100.32
Fe/Ni	717.02	836.96		786.07	982.32		1102.14				930.38	
Ni/Co	0.30	0.26		0.26	0.36		0.22				0.27	

651
652

Table 5 Representative microprobe analyses for sulfides from harzburgitic and orthopyroxenitic lithology (wt% element)

n°	Harzburgitic lithology								Orthopyroxenitic lithology			
	28	21	36	38	11	51	17	45	13	3	41	39
S	36.66	35.73	36.77	36.86	36.78	36.54	37.08	36.81	36.62	36.31	36.58	35.30
Si	0.02	0.08	0.01	0.04	0.01	0.04	0.05	0.02	b.d.	0.01	b.d.	0.04
Fe	62.99	62.36	62.83	62.53	62.74	62.82	62.22	62.17	61.60	62.29	61.78	61.88
Co	b.d.	0.04	b.d.	b.d.	b.d.	b.d.	b.d.	b.d.	b.d.	b.d.	b.d.	b.d.
Ni	0.01	0.01	b.d.	b.d.	b.d.	b.d.	b.d.	0.02	0.02	b.d.	b.d.	0.01
Mg	b.d.	0.01	0.02	0.01	b.d.	0.01	b.d.	b.d.	b.d.	0.01	b.d.	b.d.
Mn	b.d.	0.06	0.04	0.01	0.02	b.d.	0.03	0.01	0.04	b.d.	b.d.	0.03
Cr	0.01	0.03	0.08	0.02	0.04	0.07	0.11	1.57	2.29	2.34	2.42	2.82
Cu	b.d.	b.d.	b.d.	0.05	0.07	b.d.	b.d.	0.04	0.05	0.03	0.01	0.02
Sum	99.69	98.32	99.75	99.51	99.65	99.48	99.50	100.64	100.62	100.99	100.79	100.10
Fe/Ni	4531	5376	–	–	–	–	–	3342	3802	–	–	10668

653
654

Table 6 Trace element concentrations (ppm) for orthopyroxene, olivine, and chromite in NWA 4255

Lithology	Harzburgitic										
	Orthopyroxene					Olivine					
n^*	9	10	16	3	4	5	6	7	8	14	15
Ca	4972	4792	4216	–	–	1215	429	315	338	–	–
Sc	13.3	11.7	9.5	6.61	7.21	4.1	3.77	4.01	3.73	3.8	3.40
Ti	260	239	207	–	–	48.7	38	43	39.4	40.56	32.58
V	124	108	91	60.93	64.65	16.1	15.4	14	16.1	16.76	16.16
Cr	2254	1776	1331	704.27	750.63	57	58	45	53	59.05	50.31
Co	13.2	5.81	25.8	537.44	81.75	133	51	19.9	17.9	158.52	25.50
Ni	4.2	0.371	3.07	99.7	15.04	23.15	10.6	3.73	2.94	26.62	5.05
Rb	0.006	0.004	0.008	–	–	0.016	0.004	0.014	0.067	–	–
Sr	0.19	0.320	1.32	–	–	11.04	2.1	2.09	4.57	–	–
Y	0.087	0.078	0.053	0.05	0.04	0.009	0.003	0.004	0.016	–	–
Zr	0.103	0.053	0.029	0.04	0.06	0.019	b.d.	b.d.	b.d.	–	–
Nb	0.036	0.025	0.024	0.03	0.02	0.007	0.002	0.002	0.005	–	–
Ba	b.d.	b.d.	b.d.	13.06	2.81	6.321	0.949	1.604	4.698	–	–
La	0.005	0.002	0.002	0.01	0.01	0.003	0.001	0.003	0.014	–	–
Ce	0.013	0.005	0.009	–	–	0.004	0.002	0.008	0.036	–	–
Pr	0.002	0.001	0.002	–	–	0.001	b.d.	0.001	0.004	–	–
Nd	0.013	0.010	0.010	–	–	0.007	b.d.	0.004	0.016	–	–
Sm	0.005	0.005	0.006	–	–	b.d.	b.d.	b.d.	0.005	–	–
Eu	0.001	0.001	b.d.	–	–	b.d.	b.d.	b.d.	b.d.	–	–
Gd	0.009	0.008	0.006	–	–	b.d.	b.d.	b.d.	b.d.	–	–
Tb	0.002	0.001	0.001	–	–	b.d.	b.d.	b.d.	0.001	–	–
Dy	0.013	0.011	0.008	–	–	b.d.	b.d.	0.002	0.004	–	–
Ho	0.003	0.003	0.002	–	–	0.001	b.d.	b.d.	b.d.	–	–
Er	0.010	0.012	0.008	–	–	b.d.	b.d.	b.d.	0.003	–	–
Tm	0.003	0.003	0.002	–	–	0.001	b.d.	b.d.	0.001	–	–
Yb	0.021	0.022	0.017	–	–	0.002	b.d.	b.d.	0.007	–	–
Lu	0.005	0.005	0.004	–	–	0.001	0.001	0.001	0.001	–	–
Hf	0.003	0.004	0.002	–	–	0.001	b.d.	b.d.	0.002	–	–
Ta	b.d.	b.d.	b.d.	–	–	b.d.	b.d.	b.d.	b.d.	–	–
Pb	0.004	0.002	0.005	–	–	0.021	0.006	0.010	0.036	–	–
Th	0.001	b.d.	b.d.	–	–	0.001	b.d.	0.001	0.002	–	–
U	b.d.	b.d.	b.d.	–	–	0.029	0.011	0.004	0.017	–	–
Ni/Co	0.318	0.064	0.119	0.19	0.18	0.174	0.209	0.187	0.165	0.17	0.20
(La/Yb)n	0.16	0.05	0.10	–	–	0.92	–	–	1.30	–	–
(La/Sm)n	0.64	0.19	0.27	–	–	–	–	–	1.85	–	–
(Sm/Yb)n	0.25	0.26	0.36	–	–	–	–	–	0.70	–	–
Eu/Eu*	0.43	0.55	–	–	–	–	–	–	–	–	–
Ce/Ce*	3.71	3.76	4.84	–	–	3.05	–	5.16	5.10	–	–

Lithology						Orthopyroxenitic			
	Orthopyroxene					Chromite			
n^*	20	17	18	1	2	11	12	13	19
Ca	–	4969	4855	5031	4908	72	54	30	84
Sc	13.41	13.4	12.6	12.5	12.1	6.39	6.08	5.71	5.16
Ti	–	276	259	264	255	3516	3460	3640	3544
V	112.74	113	109	117	117	5469	5471	5457	5369
Cr	1666.43	1666	1664	2122	2076	376242	376242	376242	376242
Co	5.01	5.01	5.14	5.50	5.56	10.5	11.7	7.8	9.8

Ni	0.39	0.386	0.309	0.238	0.254	0.133	0.291	0.389	0.50
Rb	–	0.008	0.011	b.d.	b.d.	0.006	0.005	0.004	0.012
Sr	–	0.209	0.190	0.217	0.182	0.199	0.211	0.246	0.263
Y	–	0.098	0.094	0.145	0.137	0.016	0.018	0.018	0.019
Zr	–	0.085	0.114	0.217	0.201	3.83	3.9	3.91	3.93
Nb	–	0.025	0.026	0.040	0.029	3.73	3.75	3.67	3.93
Ba	–	0.067	0.077	b.d.	0.014	b.d.	0.016	0.066	0.126
La	–	0.002	0.003	0.002	0.002	b.d.	b.d.	b.d.	0.008
Ce	–	0.008	0.013	0.012	0.009	0.003	0.002	b.d.	0.008
Pr	–	0.002	0.002	0.003	0.003	b.d.	b.d.	b.d.	0.001
Nd	–	0.018	0.017	0.028	0.024	b.d.	b.d.	b.d.	0.013
Sm	–	0.007	0.008	0.015	0.012	0.003	b.d.	b.d.	b.d.
Eu	–	0.002	0.002	0.002	0.002	b.d.	b.d.	b.d.	b.d.
Gd	–	0.010	0.011	0.018	0.016	b.d.	b.d.	b.d.	b.d.
Tb	–	0.002	0.002	0.002	0.003	0.001	b.d.	b.d.	b.d.
Dy	–	0.014	0.015	0.022	0.024	b.d.	b.d.	b.d.	b.d.
Ho	–	0.003	0.003	0.005	0.005	b.d.	b.d.	b.d.	b.d.
Er	–	0.015	0.014	0.020	0.021	b.d.	b.d.	b.d.	b.d.
Tm	–	0.002	0.003	0.003	0.004	b.d.	b.d.	b.d.	b.d.
Yb	–	0.027	0.029	0.034	0.032	b.d.	b.d.	b.d.	b.d.
Lu	–	0.005	0.005	0.005	0.005	b.d.	b.d.	b.d.	b.d.
Hf	–	0.003	0.003	0.007	0.007	0.023	0.023	0.054	0.019
Ta	–	b.d.	b.d.	b.d.	0.001	0.008	0.009	0.002	0.008
Pb	–	0.006	0.010	0.005	0.005	b.d.	0.003	0.006	b.d.
Th	–	b.d.	0.001	b.d.	b.d.	b.d.	b.d.	b.d.	b.d.
U	–	b.d.	b.d.	b.d.	b.d.	b.d.	b.d.	b.d.	b.d.
Ni/Co	0.077	0.077	0.060	0.043	0.046	0.013	0.025	0.050	0.05
(La/Yb)n	–	0.05	0.08	0.03	0.04	–	–	–	–
(La/Sm)n	–	0.18	0.28	0.07	0.09	–	–	–	–
(Sm/Yb)n	–	0.30	0.30	0.48	0.43	–	–	–	–
Eu/Eu*	–	0.66	0.56	0.42	0.35	–	–	–	–
Ce/Ce*	–	3.41	4.59	5.14	4.13	–	–	–	2.76

Values normalized to CI chondrite (Anders and Grevesse 1989). $Eu/Eu^* = Eu_n / ((Sm_n \times Gd_n)^{1/2})$. $Ce/Ce^* = Ce_n / (La_n \times Pr_n)^{1/2})$

b.d. below detection limit

657
658

Table 7 Major and trace element compositions of whole rock from NWA 4255

	Aliquot 1 Glass bids (Nancy) (1560 mg)	Aliquot 1 ICP-AES (LMV) (1560 mg)	Aliquot 2 ICP-AES (LMV) (1570 mg)	Average	Standard deviation
Mass (mg)	5	100	100		
SiO_2 (wt%)	53.16	53.46	54.03	53.55	0.44
TiO_2	0.07	0.08	0.05	0.07	0.01
Al_2O_3	0.49	0.64	0.62	0.58	0.08
Cr_2O_3	0.56			0.56	
FeO	16.29	16.93	16.79	16.67	0.34
MnO	0.55	0.58	0.57	0.57	0.01
MgO	26.51	27.27	26.60	26.79	0.41
CaO	0.84	0.81	0.78	0.81	0.03
Na_2O	0.07	0.15	0.12	0.11	0.04
K_2O	0.05	0.17	0.12	0.12	0.06
NiO	0.02	–	–	0.02	
Sum	98.61	100.11	99.73		
	(Mntp.)	ICP-MS (LMV)	ICP-MS (LMV)		
Mass (mg)	50	98.4	100.28		
Li (ppm)	1.2	1.23	1.22	1.22	0.02
Sc	13.2	11.5	11.9	12.2	0.90
Ti	278	260	252	263	13.3
V		169	147	158	15.6
Cr		5455	3948	4701	1065
Mn		3862	3962	3912	70.7
Co	14.7	15.5	13.4	14.5	1.06
Ni	3.7	2.43	2.17	2.77	0.82
Cu	3.1	2.9	2.42	2.82	0.35
Rb	0.079	0.077	0,139	0.098	0.04
Sr	1.368	1.12	1.46	1.32	0.18
Y	0.167	0.168	0.184	0.173	0.01
Zr	0.443	0.417	0.619	0.493	0.11
Nb	0.036	0.028	0.037	0.034	0.01
Cs	0.005			0.005	
Ba	2.25	2.22	1,40	1.957	0.48
La	0.032	0.029	0.061	0.041	0.02
Ce	0.078	0.069	0.140	0.096	0.04
Pr	0.011	0.010	0.018	0.013	0.00
Nd	0.054	0.051	0.076	0.060	0.01
Sm	0.018	0.018	0.024	0.020	0.00
Eu	0.003	0.003	0.004	0.004	0.00
Gd	0.024	0.020	0.025	0.023	0.00
Tb	0.004	0.004	0.005	0.004	0.00
Dy	0.031	0.026	0.029	0.029	0.00
Ho	0.007	0.006	0.007	0.007	0.00
Er	0.025	0.019	0.022	0.022	0.00
Tm	0.004	0.004	0.005	0.004	0.00
Yb	0.037	0.038	0.033	0.036	0.00
Lu	0.008	0.006	0.007	0.007	0.00
Hf	0.014	0.013	0.020	0.016	0.00
Ta	0.002	0.002	0.002	0.002	0.00
Pb	0.067	0.066	0.134	0.089	0.04

659
660

Th	0.008		0.007		0.017		0.011	0.01
U	0.007		0.006		0.008		0.007	0.00
(La/Sm) n	1.14		1.00		1.57		1.24	0.30
(Gd/Lu) n	0.431		0.461		0.534		0.475	0.05
Eu/Eu*	0.429		0.507		0.462		0.466	0.04
Ce/Ce*	1.01		0.97		1.02		1.00	0.03

The reference of normalization is the CI chondrite (Anders and Grevesse 1989). Eu/Eu* = $(Eu_N/(Sm_N*Gd_N)^{1/2}$. Ce/Ce* = $(Ce_N/(La_N*Pr_N)^{1/2}$

661
662

663

664 **Figures Captions:**

665 Fig. 1 a Two of many fragments of NWA 4255. b, c Optical microscope photomicrographs

666 observed in reflected light showing small vugs associated with strings of sulfides (Sulf) and

667 chromium spinels (Chr) are common in the orthopyroxene (Opx) groundmass. d Mosaic

668 backscattered electron (BSE) image of orthopyroxenitic lithology of studied sample, formed

669 by orthopyroxenes and chromites. e Backscattered electron image of brecciated zone of NWA

670 4255 displaying two different types of chromium spinel, one is subhedral exhibiting irregular

671 fractures and another is euhedral, and both are surrounded by an orthopyroxene breccia. f

672 Euhedral chromium spinel within large orthopyroxene

673

674 Fig. 2 Optical microscope photomicrographs observed in reflected light of anhedral chromites

675 (Chr) associated with euhedral sulfide (Sulf) inclusions within orthopyroxene (Opx) in **a**, and

676 euhedral sulfide showing contact angle within orthopyroxene in **b**

677

678 Fig. 3 Backscattered electron (BSE) images showing textures and grain sizes of minerals

679 found in the harzburgitic and transitional lithologies of NWA 4255. a Mosaic image of a

680 brecciated fragment with large grains of olivine and iron metal. b, c Magnesian orthopyroxene

681 associated with an iron metal (Fe met) inclusion in a large olivine grain (Ol). Note that the

682 contact between orthopyroxene and olivine grains is usually nonbrecciated. d BSE image of

683 olivine-rich zone showing a close-up view of the square area indicated in a. e, f BSE images;

684 showing some rounded olivine inclusions in orthopyroxene in e. Olivine and large iron metal

685 grains within less brecciated orthopyroxene. Orthopyroxene and tiny small iron metal grain

686 occur inmore brecciated areas in f

687

688 Fig. 4 Frequency histograms for orthopyroxene and olivine Fe no. [100 Å~ Fe/(Fe + Mg) in

689 molar] in NWA 4255. Upper diagram: Two distinct populations of orthopyroxene are present.

690 Magnesian composition (harzburgitic Opx) ranges from 22.86 to 25.46 and the ferroan

691 composition (orthopyroxenitic Opx) ranges from 24.4 to 26.01. Lower diagram: olivine
692 shows two distinct populations, with a narrow composition for the large crystals and a slightly
693 larger variation for the small crystals
694
695 Fig. 5 Positive correlation between the Sc and Ti in the harzburgitic orthopyroxenes, whereas
696 orthopyroxene in the orthopyroxenitic lithology shows more restricted Ti variation
697
698 Fig. 6 Trace elements patterns for orthopyroxene from orthopyroxenitic and harzburgitic
699 lithologies of NWA 4255, normalized to Chondrites CI (Anders and Grevesse 1989)
700
701 Fig. 7 Mg#. for silicates vs Cr no. for chromite shows a comparison between this study and
702 other olivine diogenites (Irving et al. 2009)
703
704 Fig. 8 Ni versus Co diagram for olivine from NWA 4255. Compositions for NWA 4255 fall
705 on a linear trend distinct from any previously discussed in the literature. The literature data
706 used in this diagram are from: (1) Lunning et al. (2015); (2) (Shearer et al. 2010); (3) and (4)
707 (Hahn et al. 2018)
708
709 Fig. 9 Whole-rock trace elements (**a**) andREE (**b**) patterns normalized to Chondrites CI
710 (Anders and Grevesse 1989) for the NWA 4255 olivine diogenite. The abbreviations are
711 defined in Table 7
712
713 Fig. 10 Fe# for orthopyroxene vs. Fe no. for olivine from harzburgitic lithology of NWA
714 4255. The literature data used in this diagram are from (Beck and McSween 2010). The data
715 of this study falls almost exactly on the equilibrium line
716
717 Fig. 11 Ni vs. Co for olivine, orthopyroxene, metal and the whole-rock analyses of NWA
718 4255
719
720 Fig. 12 Data for NWA 4255 plotted in olivine-anorthite-quartz pseudoternary of Stopler
721 (1975), showing how olivine diogenite formation can take place at the peritectic
722
723 Fig. 13 Schematic representation illustrating the proposed model for the genesis of the NWA
724 4255, starting from the differentiation and crystallization of a magma ocean. The schematic

725 cross-section of a differentiated asteroid is based on that of Greenwood et al. (2015), using the

726 thicknesses of the various layers as given by a range of modeling studies of (Ruzicka et al.

727 1997; Righter and Drake 1997; Mandler and Elkins- Tanton 2013; Toplis et al. 2013). (See

728 text for more details)
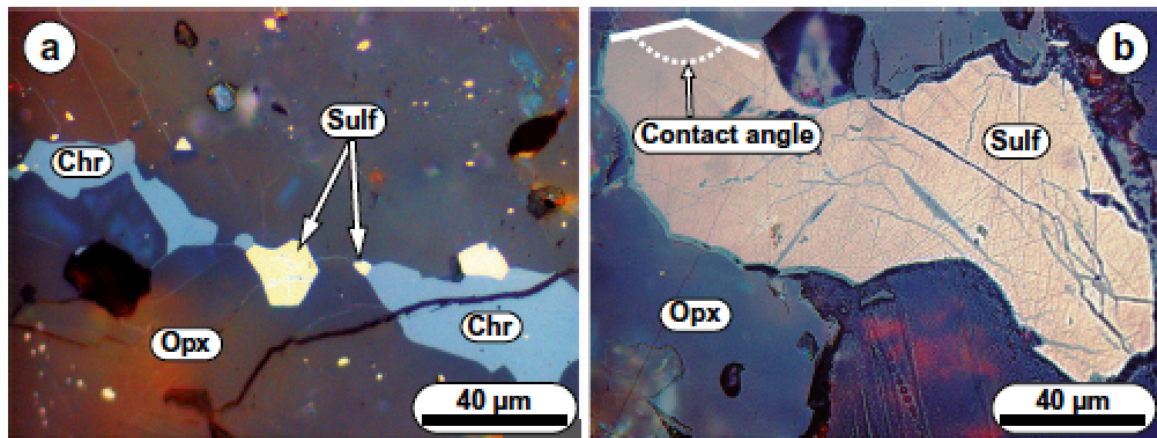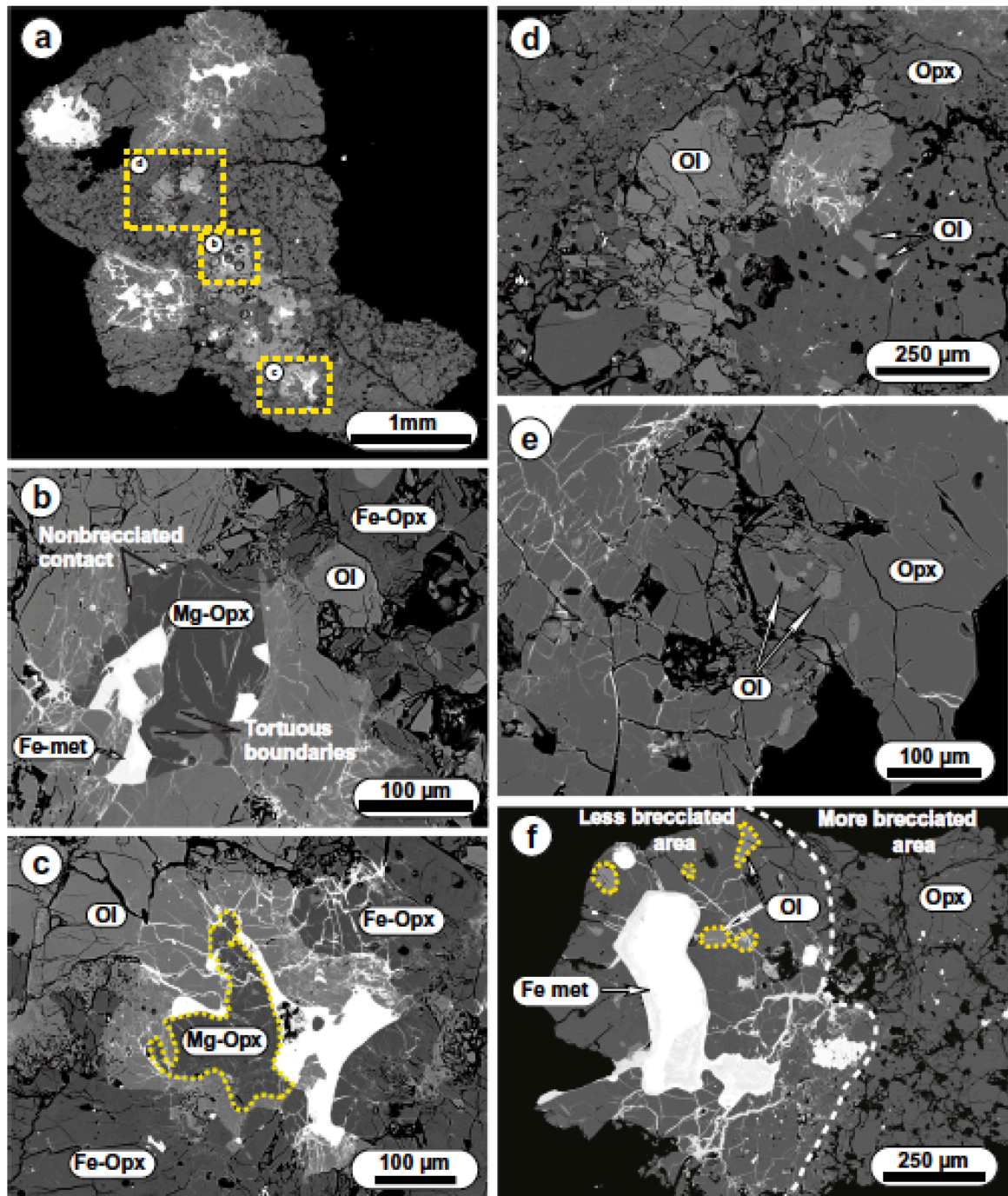
729

730

731 Fig.1
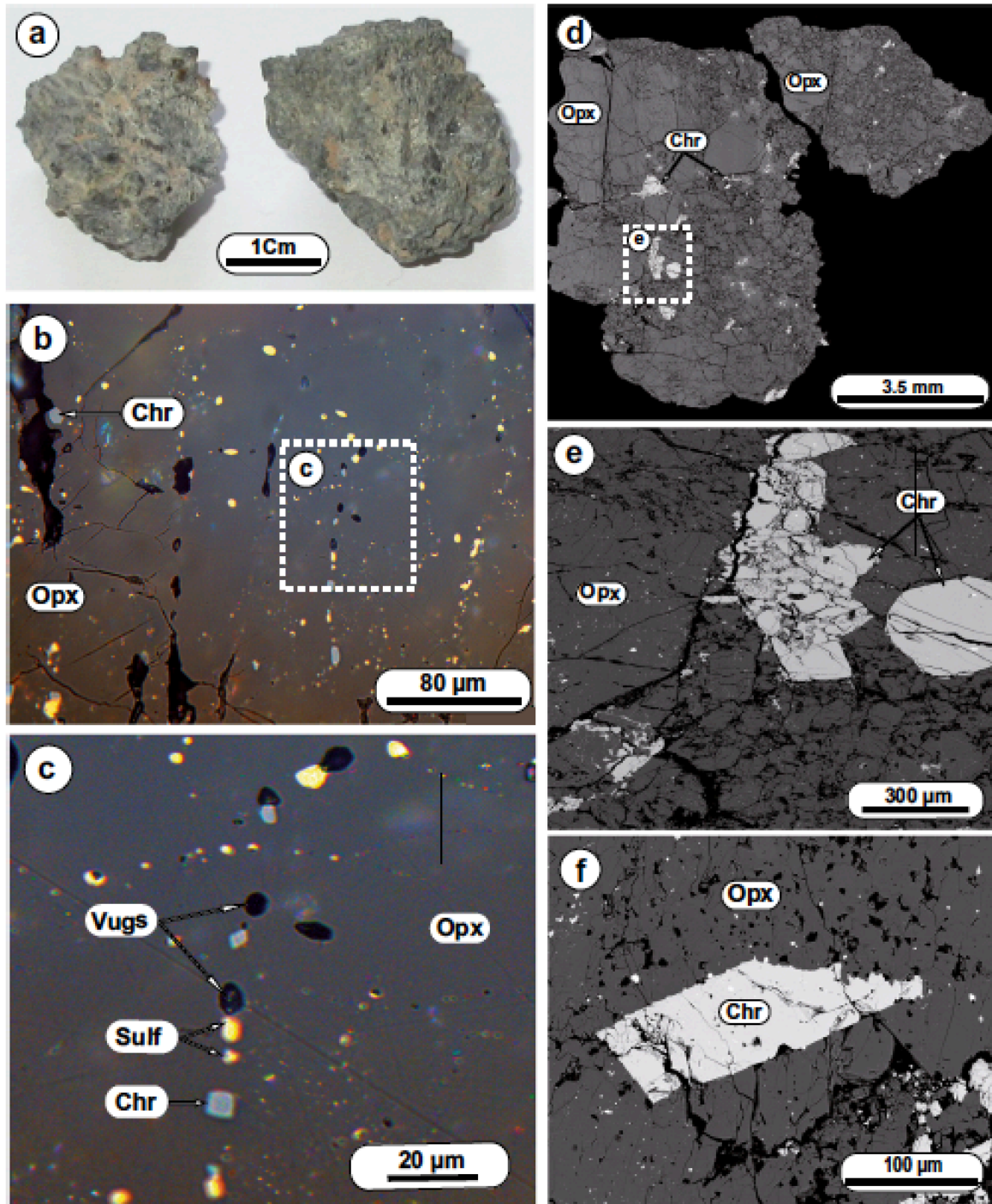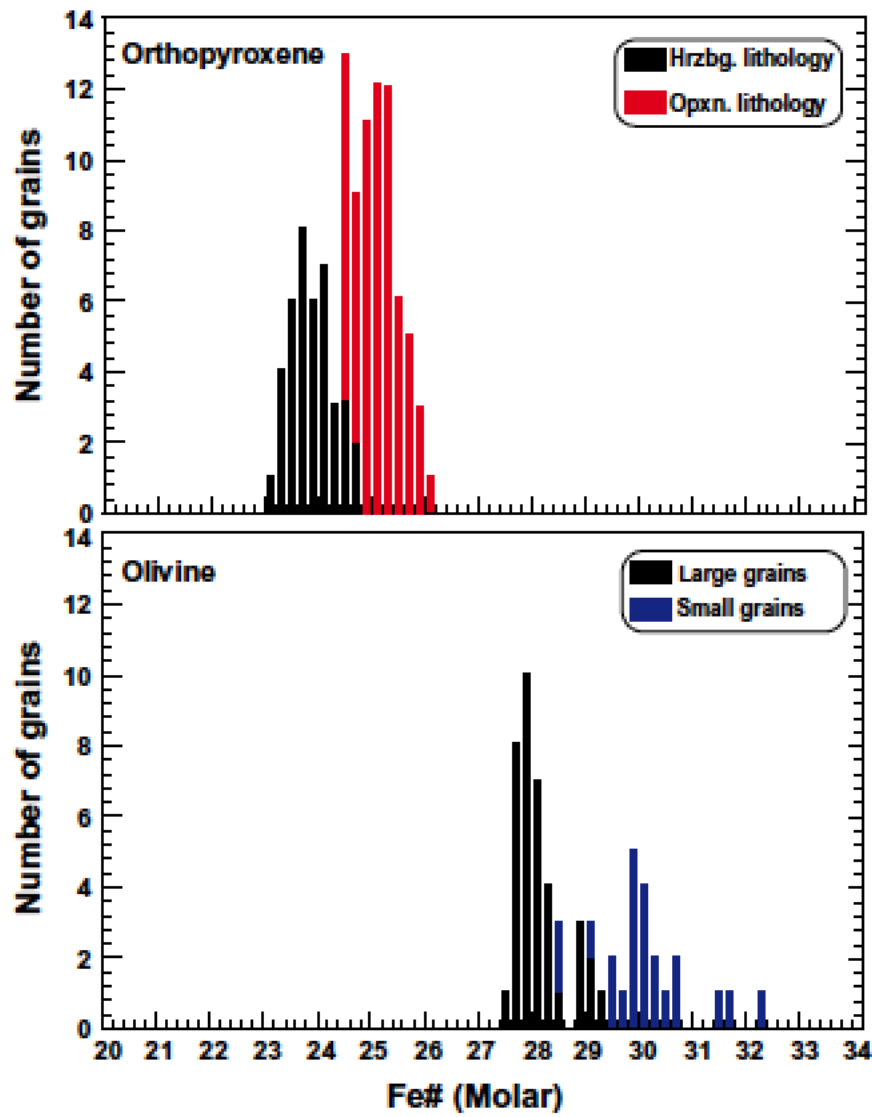

732

733

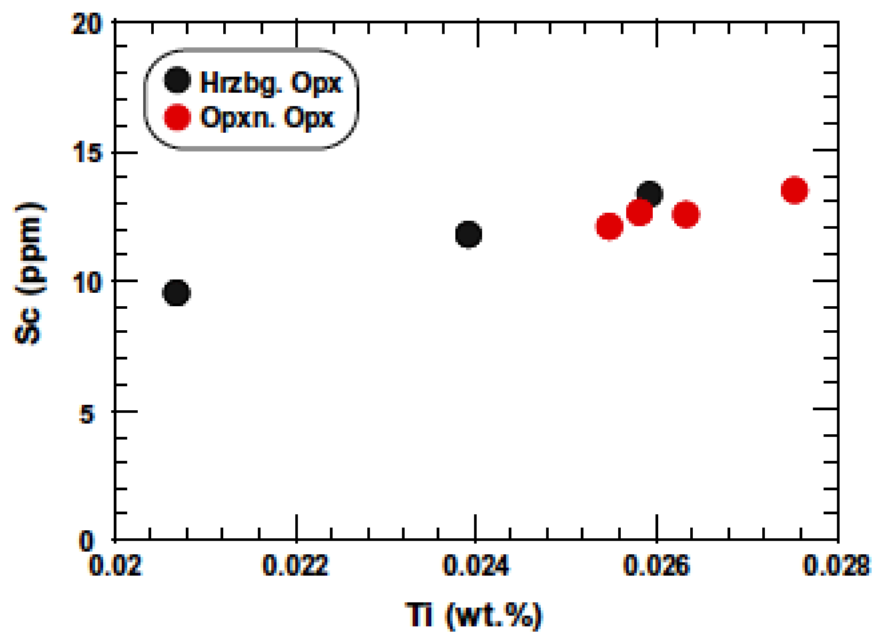734   Fig.2

735

736

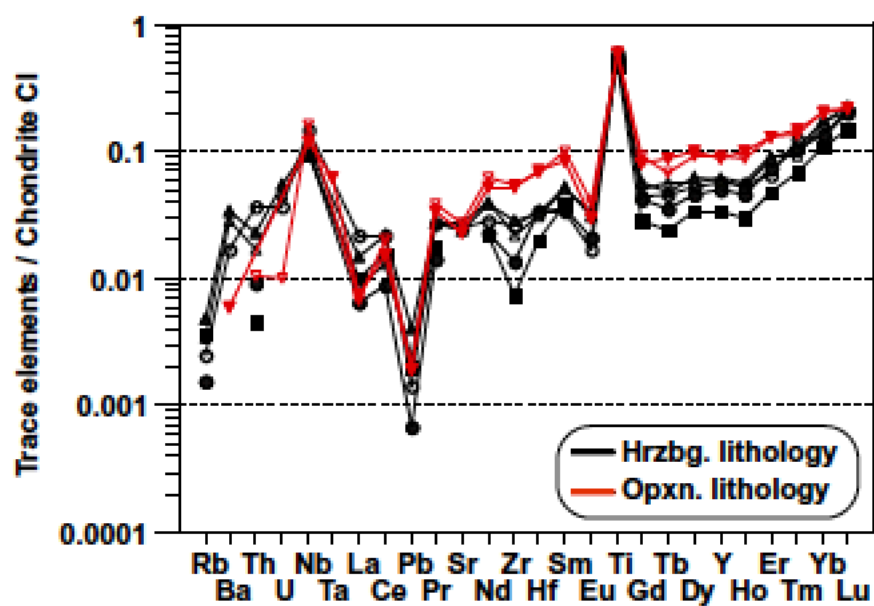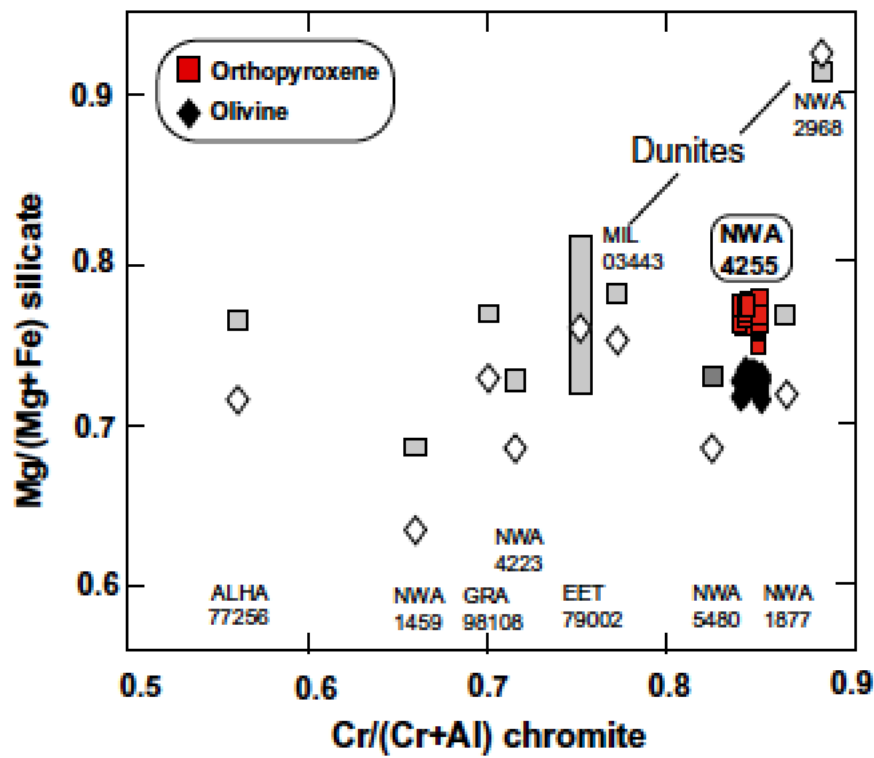737   Fig.3

738
739
740   Fig.4:

741

742

743

744   Fig.5

745

746

747   Fig.6
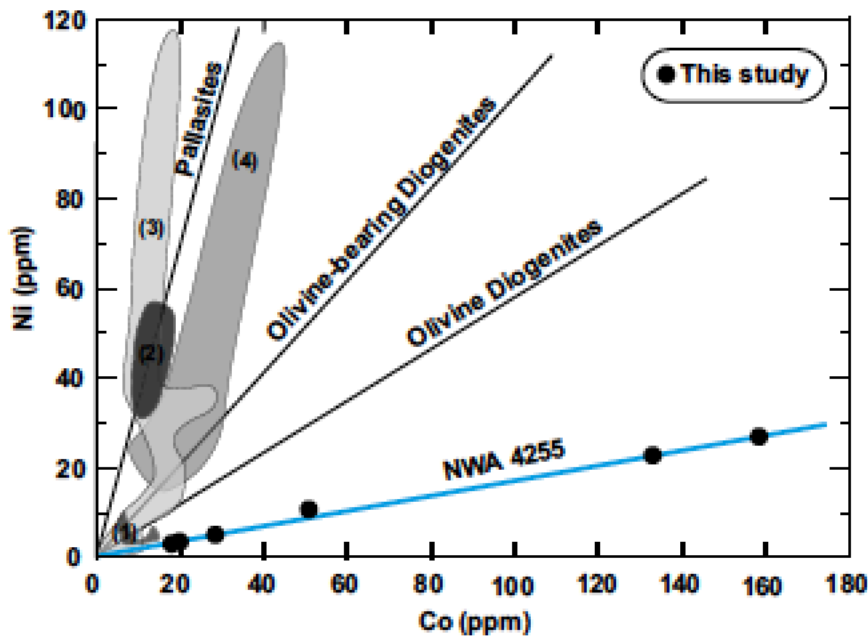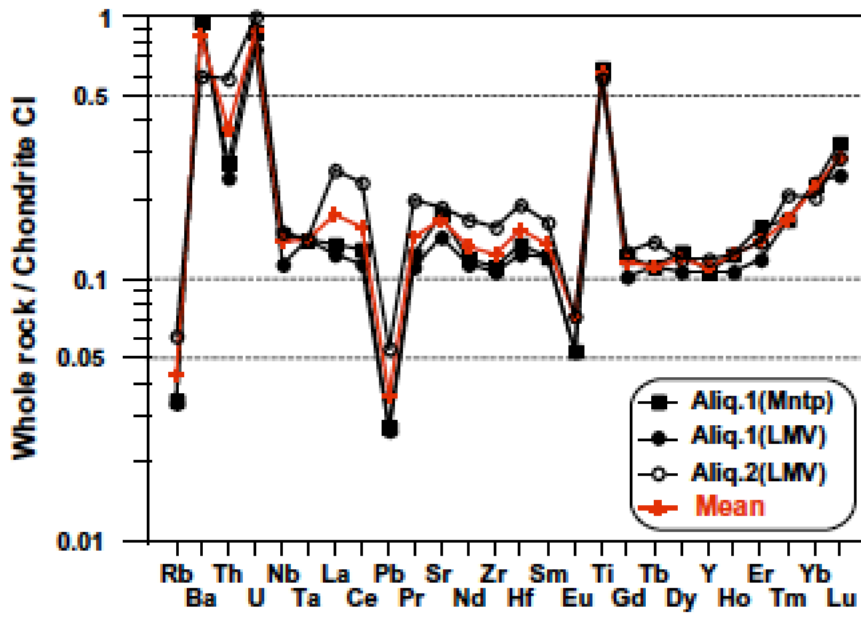

748

749

750   Fig.7

751

752

753   Fig.8
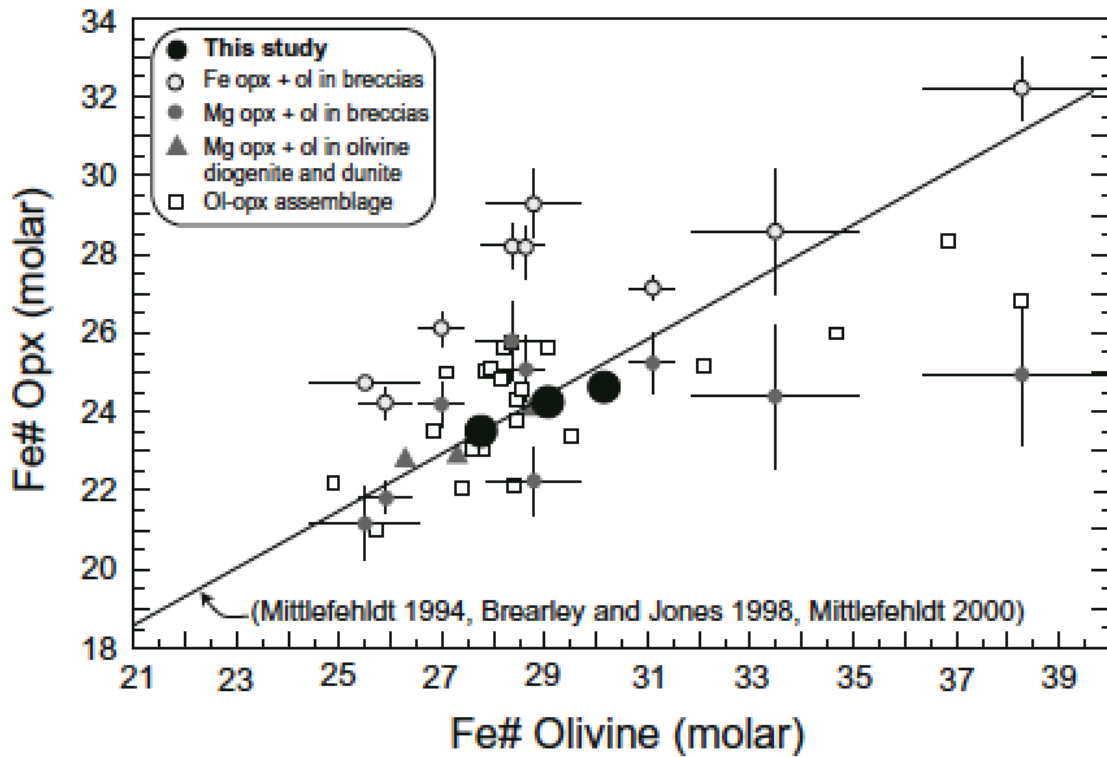

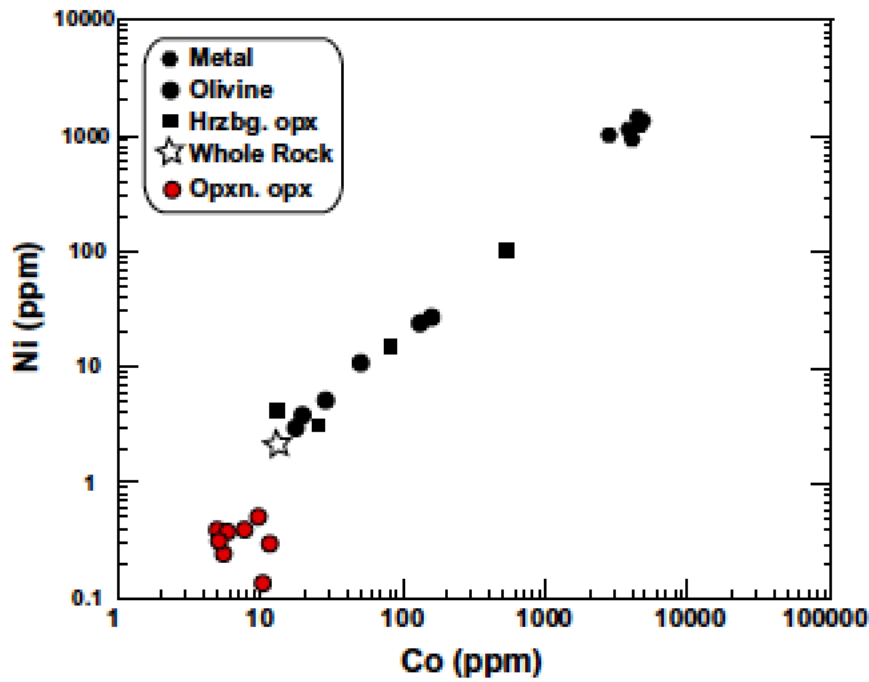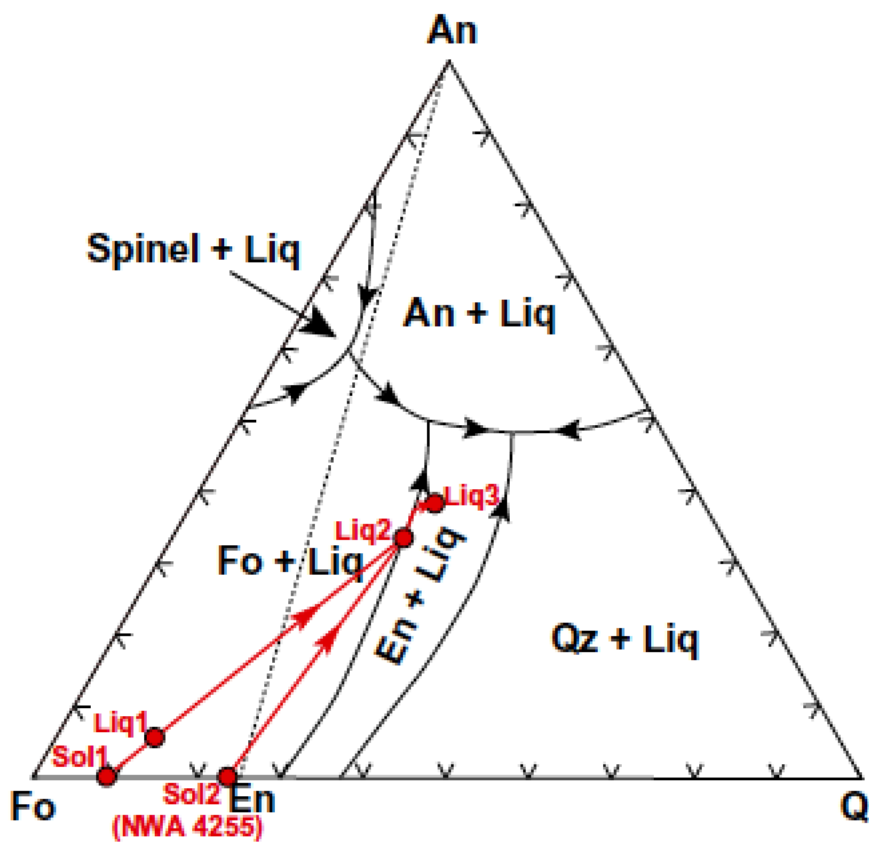
754

755

756   Fig.9

757

758

759   Fig.10

760

761

762   Fig.11

763

764

765   Fig.12

766

767

768   Fig.13

Magmatic ocean

Liquid1 (100% liquid)

70%E.C
Cooling

Basaltic upper crust

Harzburgitic Mantle

Core

Pyroxenitic lower crust

Ol
Opx1
Ol
Ol
Opx1
Ol
Ol
Opx1
Opx1
Ol
Ol
Ol
Opx1

Solid1 :
(Separate primitive mantle)

Liq
OPx1
Ol
Ol
Ol
OPx1
Ol
Ol

Residual liquid (30%)

E.C
Cooling

Peritectic reactions

Liq.2

Ol

Opx1

Liquid 2

Peritectic reactions
Opx1 and Ol
F.C of liq.2

Liq.3

Ol

Opx1

Opx 2

Liquid 3

Peritectic reactions
Opx1-Ol and
Ol-Opx2

Opx 2

ol

ol

Solid 2
(NWA 4255)

769